Development of Particle and Mesh-Particle Hybrid Methods for Multi-Phase Flow Simulations

劉, 暁星

Development of Particle and Mesh-Particle Hybrid Methods for Multi-Phase Flow Simulations

Xiaoxing LIU

Development of Particle and Mesh-particle Hybrid Methods for Multi-Phase Flow Simulations

by

Xiaoxing LIU

A thesis submitted for the degree of

Doctor of Engineering

in the Division of Engineering

Kyushu University

Department of Applied Quantum Physics and Nuclear Engineering

Kyushu University

June 2015

Contents

List of Tables

List of Figures

Chapter 1

Introduction

1.1 Review of CFD methods for multi-phase flow simulation

Multi-phase flow phenomena are frequently encountered in various engineering fields. Precise prediction of the multi-phase flow phenomena is one of the essential points to evaluate efficiency and safety of fluid power systems. With fast development of the computer science, it is now possible to numerically simulate complicated multi-phase flow problems in engineering. Up to now, Substantive efforts have been made in the computational fluid dynamics (CFD) to simulate multi-phase flow. Moving interfaces play a dominant role in these flows, and hence successful simulations depend on numerical methods that effectively capture interface features. The vast majority of CFD studies performed to address this issue have been based on Eulerian approaches. Two most commonly known Eulerian methods are the volume-of-fluid (VOF) method (Hirt and Nichols, 1981) and the level set method (Sussman et al., 1994). The method of coupled level-set with VOF (CLSVOF) (Sussman and Puckett, 2000) was also developed to correct the mass conservation of the level set method. The marker-and-cell (MAC) method (Harlow and Welch, 1965), which is one of the early-proposed front tracking methods was developed (Unverdi and Tryggvason, 1992; Tryggvason et al., 2001).

Further developments of Eulerian methods that capture fluid interfaces on a fixed grid include the constrained interpolation profile (CIP) method (Yabe et al., 2001). CIP was developed to treat both compressible and incompressible fluids with large density ratios simultaneously in one program to simulate the interaction of gas with a liquid and/or solid. CIP calculates the advection equations by interpolating the spatial

distributions of variables within an upper-wind cell by using a cubic-polynomial function; the advection equation is calculated in third order precision. The governing equations, except for the advection terms, are discretized using the finite difference method.

A developed CIP method, namely the constrained interpolated profile/multi-moment finite volume method or shortly CIP/MM FVM (Xiao, 2004), has been developed. The basic idea of the CIP/MM FVM is to make use of the cell-averaged value and the point value or even other kinds of discretized quantities simultaneously as the model variables (unknowns), which need to be memorized and predicted at every time step. A high-order CIP/MM FVM was developed (Li and Xiao., 2009). This method has been implemented in different forms to compute various fluid flows. Shallow water model was constructed by using the CIP/MM FVM (Chen and Xiao, 2008; Li and Xiao, 2010).

Though these Eulerian mesh methods have been successfully applied to study the dynamics of multiphase flows, they inevitably have a certain shortcomings.

1. Grid is necessary for most of CFD technologies. It is onerous and even troublesome in some cases to generate mesh and keep a satisfied quality of it. For example, if there is a moving or free surface in the calculation domain, an additional transport equation is calculated for grid methods to catch this surface. In addition, special cautions must be paid for preventing grids from tangling.
2. In Eulerian method, the numerical diffusion caused by the advection term is unavoidable, which will bring a numerical instability problem. Usually high-order convection scheme is applied to avoid numerical instability.

Alternative methods for multi-phase flow simulations are represented by the Lagrangian, particle-based method such as the smoothed particle hydrodynamics (SPH) method (Monaghan, 1988), the moving particle semi-implicit (MPS) method (Koshizuka, 1995) and the finite volume particle (FVP) method (Yabushita and Hibi, 2005). These

Lagrangian methods can easily analyze complex geometries and can treat viscous fluid flows without numerical diffusion caused by fluid convection. The shape of the interface is directly obtained from the set of the computational particles. As a result, no additional effort is necessary to capture or track the interface and the free surface or interface is always represented clearly in the particle-based methods.

The SPH method is a fully Lagrangian deterministic mesoscopical particle method. The SPH method was originally developed for compressible inviscid flows, such as astrophysical problems (Gingold and Monaghan, 1977). Distribution of an arbitrary quantity is presented by superposition of kernels located at particle positions. In the SPH method, motion and density of particles are explicitly simulated; pressure is thus explicitly estimated according to particle density. In contrast to Eulerian methods, grid is unnecessary at all and thus there is no numerical diffusion in the SPH method. Fluids are presented as a certain number of moving particles, whose sizes are much larger than a molecule one. Fluid properties are deterministically given. As a result, calculation load is smaller than those of microscopical methods. The SPH method has been extensively studied during past twenty years. It has been successfully and widely applied. Because of success of the SPH method, moving particle methods presently become one of focuses in researches of the CFD.

The MPS method (Koshizuka et al., 1995) is a fully Lagrangian deterministic mesoscopical particle method, which was original invented for incompressible viscous fluids with free surface. In the MPS method, the motion of each particle is calculated through interactions with neighboring particles covered with a kernel function. All terms in the govern equations, such as gradient and Laplacian terms, are represented by the deterministic particle interaction models. With a MAC algorithm, calculations in the MPS method are separated into two stages: in the explicit stage, particles move with all

external force except pressure; in the implicit stage, velocities and positions of particles are updated according to implicitly solved pressure of a pressure Poission equation by keeping a constant particle number density. Due to a fully Lagrangian particle method, numerical diffusion is avoid and free surface is clear all the time. The MPS method has been proved to a robust technology for solving complicated phenomena. Flow phenomena with large deformation of fluids can be easily simulated by the MPS method, for example the dam-break problem (Koshizuka and Oka, 1996), water impingement and splashing on a pipe surface (Koshizuka et al., 1998). With a surface tension model based on the continuum surface force (CSF) model, droplet breakup was simulated and analyzed using the MPS method (Nomura et al., 2001; Duan et al., 2003). The MPS method was also applied to simulate a liquid droplet impacting on a liquid film (Xie, et al., 2004, 2005). Multi-phase flow problems with/without phase change can be also simulated using the MPS method. Then there are lots of researches focusing on the stability of MPS method. A particle interaction kernel was developed for convection-diffusion scalar transport equation (Huang et al., 2011). Modified Poison pressure equation and a modified pressure gradient model were presented to enhance the stability and accuracy of the moving particle semi-implicit method (Khayyer and Gotoh, 2011).

Compared to the MPS method, the FVP method can evaluate the pressure more reasonably and thus it is numerically more stable (Yabushita and Hibi, 2005). In addition, this method needs no special treatment for moving particles on the free surface. Coupled with a pressure-based semi-implicit solver, CUP (Combined, Unified Procedure) algorithm, the FVP method has successfully simulated single bubble rising up in a stagnant liquid pool for large density and viscosity ratios between gas and liquid phases up to 100 (Zhang et al., 2008). However, this approach cannot solve numerical difficulties in simulations with larger differences in physical properties between two phases.

Several recent studies have been devoted to mix Eulerian and Lagrangian numerical methods designed for solving Eulerian interface tracking. A hybrid method based on the MPS method was developed (Liu et al., 2005). In this hybrid method one phase is defined on a stationary mesh and the other phase is represented by moving particles that sharply capture the dynamics of the interface. In this method, as particles are used to represent one phase, the computation cost will increase dramatically compared with conventional mesh methods. Another hybrid method coupling CIP and MPS was also developed (Ishii et al., 2006, 2011). With this hybrid method, velocities given by the advection part of the particle method were combined with those given by the advection part of the CIP. However, its numerical solution algorithm does not employ tight coupling between the mesh and particle methods. This would lead to numerical inconsistency in fluid properties represented by particles and mesh.

1.2 Objective and outline of the present study

For design and safety of nuclear reactors, we have to analyze complex thermal-hydraulic problems, and most of phenomena involved in these problems are multi-phase flows with large deformation of phase interfaces. As fully Lagrangian particle methods, moving particle methods can implicitly track the phase interface. In addition, there are no numerical diffusions arising on the interfaces since no convection term is required in moving particle methods.

The FVP method has been developed as a powerful tool based on a fully Lagrangian particle method. It has been applied to simulate multi-phase flow and phase change phenomena. However, there are still some problems needed to be solved for practical application of the FVP method. Numerical instability problems occurred in the simulations using the FVP method due to unphysically solved pressures in particular for

flows with a large density ratio between two phases. In addition, compared with mesh-method calculations, the particle-based methods need a large calculation resource to perform simulations on a similar scale. To solve these problems occurring when applying the FVP method, it should be developed with stable pressure solution algorithm and a mesh-particle hybrid method is believed to be able to achieve efficient and accurate calculation.

In this study, a two-step pressure algorithm will be developed to cope with the pressure instability caused by sharp jump of physical properties between different phases. A model to improve the sharpness of the interface will also be introduced. Simulations of two experiments for single bubble rising in a tank of stagnant liquid and a tank of solid particle-liquid mixture will be performed to validate the developed computational framework. However, the computation cost of this two-step FVP method is still high and it diminishes the accuracy since the pressure equation for different phases are solved separately.

Further, since the mesh method can simulate multi-phase flow with stable pressure solution and low computation cost, to conquer the problem when we simulate multi-phase flows using the FVP method, a mesh-particle hybrid method will be developed for efficient and accurate simulations of multi-phase flows. The hybrid method couples the CIP/MM FVM and the FVP method. The main part of flows is solved by the CIP/MM FVM, while the interface between two phases is captured by the FVP method. Numerical particles in the FVP method are distributed only on the surface of liquid to capture the interface between liquid and gas phases, and the particles are used to determine fluid density of each mesh grid. As the CIP/MM FVM uses both volume integrated average (VIA) and the surface integrated average (SIA) of the physical variable and it enables to

make high order reconstruction with less mesh stencils, the developed hybrid method enables accurate and efficient multi-phase flow simulation.

Fundamental applicability of the develop hybrid method to the multi-phase flow simulation will be validated through three adiabatic benchmark calculations of the dam break, single bubble rising in the stagnant liquid and droplet breakup. The results of simulations using the hybrid method will be compared with results calculated by those obtained by other numerical method and available experimental results.

Two-phase flow phenomena accompanying phase change phenomenon are very important in nuclear safety analysis and the hybrid method is very suitable to solve this phenomena. The heat transfer model will be developed for this mesh-particle hybrid method. The so-called Stefan problem and the horizontal film boiling will be used to validate the model implemented into the hybrid method. Simulation results of Stefan problem will be compared with analytical result and simulation results of horizontal film boiling will be compared with those calculated by the VOF method.

It is difficult for the FVP method to simulate compressible flow. However, as the mesh method can simulate compressible flow easily, the present mesh-particle hybrid method will also be extended to calculate incompressible and compressible flows simultaneously. Compression of a gas bubble in liquid phase will be calculated and the result will be compared with analytical results.

The present thesis is divided into six chapters. The first chapter focuses on the background and objective of the study. The second chapter is allocated to the basic mathematical description of the FVP method and the extension of the FVP method to multi-phase flow simulations. Subsequently, simulation of gas-liquid and gas-liquid-solid multi-phase flows using the two-step pressure algorithm is presented and its validation is discussed based on the comparison between experiments and simulation results in the

third part. In the fourth part, a mesh-particle hybrid method is described. The hybrid method couples the CIP/MM FVM and the FVP method. In the fifth part, simulations of flows with interface deformation, heat transfer and compressible flows are presented to validate the hybrid method. Finally, the present study and future work is indicated.

Chapter 2

Development of Particle-Based Simulation Method

2.1 Overview of finite volume particle (FVP) method

The full set of governing equations for incompressible viscous flows consists of the Navier-Stokes (N-S) equation and the equation of continuity:

$$\frac{D\vec{u}}{Dt} = -\frac{1}{\rho}\left[\nabla p + \mu\nabla^2\vec{u} + \vec{g} + \vec{f}\right], \tag{2.1}$$

$$\nabla\cdot\vec{u} = 0. \tag{2.2}$$

where $\vec{u}$ is the velocity, t the time, ρ the density, μ the viscosity, p the pressure, $\vec{g}$ the gravitational force, and $\vec{f}$ represents other forces such as surface tension.

For the incompressible flow, the pressure is always solved through the following Poisson equation which is derived by combining mass and momentum equations:

$$\nabla\cdot\left(\frac{1}{\rho}\nabla p^{n+1}\right) = \frac{\nabla\cdot\vec{u}^*}{\Delta t}. \tag{2.3}$$

where p^{n+1} is the pressure of time step of $n+1$, $\vec{u}^*$ is the intermediate velocity, Δt is the time step size.

In the FVP method, the calculation domain is represented by a set of discrete numerical particles, which are not only the interpolation points, but also carry the material properties. The velocity of each particle is calculated through interactions with neighboring particles covered with a kernel function. The neighboring particle interactions schematically can be seen in Figure 2.1-1. All terms in governing equations, such as gradient and Laplacian terms, are discretized using a deterministic particle interaction model, which will be simply introduced in the following.

The numerical particles, which are used to discretize governing equations, are assumed to occupy a certain volume, where the control volume of one moving particle is a circle in 2D simulations:

$$S = 2\pi R\,,\ V = \pi R^2 = (\Delta l)^2\,, \qquad \text{for 2D} \tag{2.4}$$

where S, V, R and Δl are the particle surface area, the particle control volume, the radius of particle control volume and the initial particle distance, respectively.

$$\Delta l \approx 2R \tag{2.5}$$

According to Gauss's law, the gradient and Laplacian operators acting on arbitrary scalar function ϕ are expressed by

$$\nabla\phi = \lim_{R\to 0}\frac{1}{V}\iiint_V \nabla\phi dV = \lim_{R\to 0}\frac{1}{V}\iint_S \nabla\phi\vec{n}dS\,, \tag{2.6}$$

$$\nabla^2\phi = \lim_{R\to 0}\frac{1}{V}\iiint_V \nabla^2\phi dV = \lim_{R\to 0}\frac{1}{V}\iint_S \nabla\phi\cdot\vec{n}dS\,, \tag{2.7}$$

where the gradient and Laplacian terms of particle can be approximated as

$$\left\langle\nabla\phi\right\rangle_i = \left\langle\frac{1}{V}\iint_S \nabla\phi\vec{n}dS\right\rangle_i = \frac{1}{V}\sum_{j\neq i}\phi_{sur}\cdot\vec{n}_{ij}\cdot\Delta S_{ij}\,, \tag{2.8}$$

$$\left\langle\nabla^2\phi\right\rangle_i = \left\langle\frac{1}{V}\iint_S \nabla\phi\cdot\vec{n}dS\right\rangle_i = \frac{1}{V}\sum_{j\neq i}\left(\frac{\phi_j-\phi_i}{\left|\vec{r}_{ij}\right|}\right)\cdot\Delta S_{ij}\,, \tag{2.9}$$

where $\left\langle\phi\right\rangle_i$ is the approximation of ϕ with respect to particle i and $|\vec{r}_{ij}|$ is the distance between particles i and j, and $\vec{n}$ is the unit vector.

Since the gradients of arbitrary function (velocity and pressure) are computed on the surface of each particle, the function values for ϕ_{sur} are obtained by using linear reconstruction as the following equation:

$$\phi_{sur} = \phi_i + \frac{\phi_j-\phi_i}{|\vec{r}_{ij}|}R\,. \tag{2.10}$$

Since the finite volume particles are assumed to occupy the same volume, to ensure that the kernel function forms a partition of unity, the interaction surface of particle i with j, ΔS_{ij}, can be calculated by

$$\Delta S_{ij} = \frac{\omega_{ij}}{\sum_{j \neq i} \omega_{ij}} S \,. \tag{2.11}$$

Figure 2.1-2 schematically shows the 2D interactions between finite volume particles. The kernel function between particle i and j in the FVP method is defined by a compactly supported form

$$\omega_{ij} = \begin{cases} \sin^{-1}\left(\frac{R}{|\vec{r}_{ij}|}\right) - \sin^{-1}\left(\frac{R}{r_e}\right) & |\vec{r}_{ij}| \le r_e \\ 0 & |\vec{r}_{ij}| \ge r_e \end{cases}, \tag{2.12}$$

where r_e denotes the radius of interaction domain which is called as "the cut-off radius", which is chosen as 4.1 Δl for a 2D system. This cut-off radius is used to define the limitation area of neighboring particles around particle i. For the incompressible flows, the number density for every particle retains constant as so-called "initial particle number density" n^0 expressed by

$$n^0 = \sum_{j \neq i} \omega_{ij} \,, \tag{2.13}$$

where the summation excludes the particles on the free surface and wall boundary. Through these neighboring fluid particle interactions, the fluid movement and heat and mass transfer are modeled.

The integral forms of Eqs. (2.1) and (2.2), respectively, are

$$\frac{D}{Dt}\int_V \vec{u} dV = -\frac{1}{\rho}\oiint_S p \cdot \vec{n} dS + \frac{1}{\rho}\oiint_S (\mu \nabla \cdot \vec{u}) \cdot \vec{n} dS + \int_V \vec{g} dV + \int_V \vec{f} dV \,, \tag{2.14}$$

$$\oiint_S \vec{u} \cdot \vec{n} dS = 0 \,, \tag{2.15}$$

By using Eqs. (2.8) and (2.9), the integral form of N-S equation, Eq. (2.14), can be discretized as

$$\left(\frac{D\vec{u}}{Dt}\right)_i = -\frac{1}{\rho\pi R^2}\sum_{j=1,j\neq i}\left(\mathrm{p_i}+\frac{\mathrm{p_j}-\mathrm{p_i}}{\left|\vec{\mathrm{r}}_{\mathrm{ij}}\right|}\mathrm{R}\right)\Delta S_{ij}\vec{n}_{ij}+\frac{\upsilon}{\pi R^2}\sum_{j=1,j\neq i}\frac{\vec{u}_{\mathrm{j}}-\vec{u}_{\mathrm{i}}}{\left|\vec{\mathrm{r}}_{\mathrm{ij}}\right|}\Delta S_{ij}+\vec{g}+\vec{f}\ . \quad (2.16)$$

2.1.1 Solution algorithm

A conventional semi-implicit algorithm is applied to solve the governing equations in the FVP method. First, the particle's intermediate velocity and position are estimated in an explicit step without the pressure force:

$$\vec{u}^{*}=\vec{u}^{n}+\Delta t\frac{1}{\rho}\left[\mu\nabla^2\vec{u}^{n}+\vec{g}+\vec{f}^{n}\right], \quad (2.17)$$

$$\vec{r}^{*}=\vec{r}^{n}+\Delta t\cdot\vec{u}^{*}, \quad (2.18)$$

The pressure filed could be solved in the solution of the Poisson equation Eq. (2.3) to obtain a divergence free velocity field implicitly. It can be seen that the implicit pressure correction is analogous to that of simplified marker and cell (SMAC) method (Amsden and Harlow, 1970) in grid-based methods. The linear equations are solved by the incomplete Cholesky decomposition conjugate gradient (ICCG) method.

Then the correction velocity is updated as

$$\vec{u}^{n+1}=\vec{u}^{*}-\Delta t\frac{1}{\rho}\nabla p^{n+1}, \quad (2.19)$$

$$\vec{r}^{n+1}=\vec{r}^{n}+\Delta t\cdot\vec{u}^{n+1}. \quad (2.20)$$

Figure 2.1-3 shows the explicit-implicit solution algorithm used in the FVP method.

To obtain the stable resolution process, the Courant–Friedrichs–Lewy (CFL) condition is brought into to control the time step size (Zhang et al., 2009):

$$\max\left\{\frac{abs\left[\left(\vec{u}_j-\vec{u}_i\right)\cdot\vec{n}_{ij}\right]\Delta t}{\left|\vec{r}_{ij}\right|}\right\}<\xi, \quad (2.21)$$

where the parameter ξ is usually chosen as 0.2.

2.1.2 Boundary condition

It is necessary to consider how to represent the boundary conditions in the FVP method, since the cut off radius would not be compatible with geometry boundaries. The wall boundary and the free surface boundary that are implemented into the system will be described in the following.

(a) Wall boundary

In the present study, the virtual or dummy particles are utilized to provide the flexibility of direct application of the Dirichlet and Neumann conditions to the boundary, which are required by a physical problem. The particles are generated by reflecting fluid particles to the wall. Hence no need to present fixed outer particles in order to satisfy the number of density calculation of wall and nearby fluid particles. Fluid particles interact with wall particles, dummy particles and other fluid particles that are in its support domain according to the cut-off radius. The illustration of this treatment can be seen in Figure 2.1-4.

(b) Free surface boundary

Particle contacting in the free surface is estimated with the following equation, which is discretization form of Poisson equation:

$$\frac{1}{\rho_i}\sum_{j=1,j\neq i}\frac{p_j-p_i}{\left|\vec{r}_{ij}\right|}\Delta S_{ij}+\frac{p_{free}-p_i}{\rho R}\left|\Delta S_{free}\right|$$
$$=\frac{1}{\Delta t}\sum_{j=1,j\neq i}\left(\vec{u}_i+\frac{\vec{u}_j-\vec{u}_i}{\left|\vec{r}_{ij}\right|}R\right)\cdot\Delta S_{ij}\vec{n}_{ij}+\frac{1}{\Delta t}\left[\vec{u}_i+\left(\frac{\partial\vec{u}}{\partial n}\right)_{free}R\right]\cdot\Delta S_{free}\vec{n}_{ij}, \qquad (2.22)$$

where p_{free} is the pressure on the free surface, and $\left(\frac{\partial\vec{u}}{\partial n}\right)_{free}$ is the velocity gradient on the free surface.

By the approximation of the zero Dirichlet and homogenous Neumann conditions for pressure p_{free} and velocity divergence $\left(\frac{\partial \vec{u}}{\partial n}\right)_{free}$, respectively, Eq. (2.23) will be

$$\frac{1}{\rho}\sum_{j=1,j\neq i}\left(\frac{p_j-p_i}{\left|\vec{r}_{ij}\right|}\right)\Delta S_{ij}-\frac{p_i}{\rho R}\left|\vec{S}_{free}\right|=\frac{1}{\Delta t}\sum_{j=1,j\neq i}\left(\vec{u}_i+\frac{\vec{u}_j-\vec{u}_i}{\left|\vec{r}_{ij}\right|}R\right)\cdot\Delta S_{ij}\vec{n}_{ij}+\frac{1}{\Delta t}\vec{u}_i\cdot\vec{S}_{free}, \quad (2.23)$$

where the vector $\vec{S}_{free}$ is refered to the interaction surface on free surface that can be calculated as follows:

$$\vec{S}_{free}=-\sum_{j\neq i}\Delta S_{ij}\cdot\vec{n}_{ij}. \quad (2.24)$$

Thus, the Laplacian and gradient of the pressure, as well as the divergence of the velocity for the particles on the free surface, can be expressed as

$$\nabla^2 p_i=\frac{1}{V}\left(\sum_{j\neq i}\frac{p_j-p_i}{\left|\vec{r}_{ij}\right|}\Delta S_{ij}-\frac{p_i}{R}\left|\vec{S}_{free}\right|\right), \quad (2.25)$$

$$\nabla p_i=\frac{1}{V}\left(\sum_{j\neq i}\frac{p_j+p_i}{2}\Delta S_{ij}\vec{n}_{ij}+\frac{p_i}{2}\vec{S}_{free}\right), \quad (2.26)$$

$$\nabla\cdot\vec{u}_i=\frac{1}{V}\left(\sum_{j\neq i}\left(\vec{u}_i+\frac{\vec{u}_j-\vec{u}_i}{\left|\vec{r}_{ij}\right|}R\right)\cdot\Delta S_{ij}\vec{n}_{ij}+\vec{u}_i\cdot\vec{S}_{free}\right). \quad (2.27)$$

The treatment of the boundary condition for particle i lying on the free surface is shown in Figure 2.1-5.

2.2 Extension to multi-phase flow simulations

2.2.1 Surface tension model

For the simulations of gas-liquid two-phase flows, the force from surface tension acting on the gas-liquid interface is represented by a model based on the surface free energy (Kondo et al., 2007). This model is highly applicable to particle-based methods because the

surface tension is calculated as an attractive force based on the potential energy defined for particle i and a neighboring particle j as

$$P(|\vec{r}_{ij}|) = Ce(|\vec{r}_{ij}|), \tag{2.28}$$

with

$$e(|\vec{r}_{ij}|) = \begin{cases} \frac{1}{3}(|\vec{r}_{ij}| - \frac{3}{2}\Delta l + \frac{1}{2}r_e)(|\vec{r}_{ij}| - r_e) & |\vec{r}_{ij}| < r_e \\ 0 & |\vec{r}_{ij}| \geq r_e \end{cases}, \tag{2.29}$$

and parameter C obtained from the surface tension coefficient σ:

$$C = 2\frac{(\Delta l)^2}{\sum_{j \neq i} e(|\vec{r}_{ij}|)}\sigma. \tag{2.30}$$

As a result, the surface tension acting on particle i can be calculated as

$$\vec{f}_i = \sum_{j \neq i}\vec{f}_{ij} = -\sum_{j \neq i}\frac{C}{\rho(\Delta l)^3}\frac{\partial e(|\vec{r}_{ij}|)}{\partial |\vec{r}_{ij}|}\vec{r}_{ij}, \tag{2.31}$$

where $\vec{f}_{ij}$ is the interaction force due to the potential energy between particle i and j given by

$$\vec{f}_{ij} = -\sum_{j \neq i}\frac{1}{\rho(\Delta l)^3}\frac{\partial P(|\vec{r}_{ij}|)}{\partial |\vec{r}_{ij}|}\vec{r}_{ij}. \tag{2.32}$$

2.2.2 Overview of the distinct element method (DEM)

In order to simulate gas-liquid-solid three phase flows, calculation of interactions between solid particles is necessary. The governing equations for the solid particles, which are assumed rigid, are the equations of rectilinear and rotational motion:

$$m\frac{D\vec{u}}{Dt} = \vec{F}_{col} + \vec{F}_f + \vec{F}_g \tag{2.33}$$

$$I\frac{D\vec{\omega}}{Dt} = \vec{T}_{col} \tag{2.34}$$

where m is the mass, $\vec{F}_{col}$ the contact force with neighboring solid particles or the wall, $\vec{F}_f$ the total particle-fluid interaction force, and $\vec{F}_g$ the gravitation force. The variables I, $\vec{\omega}$, and $\vec{T}_{col}$ are momentum of inertia, angular velocity, and torque, respectively.

The distinct element method (DEM) employs a viscoelastic contact model (Balevičius et al, 2008) for calculations of the contact force between solid particles. As solid particles move, they may collide with neighboring particles or the wall. Each contact is represented by a set of normal and shear springs, normal and shear dashpots, and a shear slider, which determine the contact force acting on the solid particle. The contact force between particles i and j is expressed in terms of the normal and tangential components:

$$\vec{F}_{ij} = \vec{F}_{n,ij} + \vec{F}_{t,ij} . \tag{2.35}$$

The normal component of the contact force $\vec{F}_{n,ij}$ can be evaluated based on Hooke's law:

$$\vec{F}_{n,ij} = \frac{4}{3}\frac{E_i E_j}{E_i(1-\nu_j^2)+E_j(1-\nu_i^2)} R_{ij} h_{ij} \vec{n}_{ij} - \gamma_n m_{ij} \vec{u}_{n,ij} , \tag{2.36}$$

where $m_{ij} = m_i m_j / (m_i + m_j)$ and $R_{ij} = R_i R_j / (R_i + R_j)$ represent the reduced mass and reduced radius of particles i and j, respectively, E the elastic modulus, ν Poisson's ratio, γ_n the viscous damping coefficient in the normal direction, and $h_{ij} = R_i + R_j - |\vec{r}_{ij}|$ the overlap length between contacting particles i and j. The tangential force $\vec{F}_{t,ij}$ is specified by distinguishing the tangential force produced by static and dynamic friction:

$$\vec{F}_{t,ij} = -\vec{t}_{ij} \min(|F_{t,ij,static}|, |F_{t,ij,dynamic}|) , \tag{2.37}$$

where $\vec{t}_{ij}$ is the unit tangential vector. The static friction force can be modeled as

$$F_{t,ij,static} = \frac{16}{3} G_i G_j \sqrt{\frac{R_{ij} h_{ij}}{G_i(2-\vec{\nu}_j)+G_j(2-\vec{\nu}_i)}}\vec{\delta}_{ij} - \gamma_t m_{ij} \vec{u}_{t,ij} , \tag{2.38}$$

where G is the respective shear modulus, $\vec{\delta}_{ij}$ the integrated tangential displacement vector, and γ_t the viscous damping coefficient in the tangent direction. The dynamic friction force is expressed by Coulomb's friction law:

$$\vec{F}_{t,ij,dynamic} = -\eta(|\vec{F}_{n,ij}|)\vec{t}_{ij}, \tag{2.39}$$

where η is the friction coefficient.

The FVP method and DEM are combined to directly simulate the solid–fluid mixture flows. A multiple time step algorithm is introduced (Zhang et al., 2006). Combining the calculations is outlined schematically in Figure 2.2-1.

2.2.3 Improvement of numerical stability

(a) Two-step pressure solution algorithm

In the present study, to overcome the numerical difficulties caused by large differences in physical properties between liquid and gas phases, we use a two-step method to solve the Poisson pressure equation. In the two-step method, first, temporal pressure p^* of the liquid phase is calculated solving the following Poisson pressure equation for liquid numerical particles with the pressure of gas numerical particles adjacent to the liquid numerical particles as the boundary condition:

$$\left\langle \nabla \cdot \left(\frac{1}{\rho} \nabla p^* \right) \right\rangle_l = \frac{\left\langle \nabla \cdot \vec{u}^* \right\rangle_l}{\Delta t}, \tag{2.40}$$

where p_l^* is the pressure at the first step of the pressure calculation; subscript *l* indicates averaging over the liquid phase. The temporal velocity of liquid numerical particles is then calculated and the temporal position of liquid numerical particles is updated:

$$\vec{u}_l^{**} = \vec{u}_l^{*} - \Delta t \frac{1}{\rho} \nabla p^{n+1}, \tag{2.41}$$

$$\vec{r}_l^{*} = \vec{r}_l^{n} + \Delta t \cdot \vec{u}_l^{n+1}. \tag{2.42}$$

The Poisson pressure equation for gas numerical particles is then calculated from

$$\left\langle \nabla \cdot \left(\frac{1}{\rho} \nabla p^{**} \right) \right\rangle_g = \frac{\left\langle \nabla \cdot \vec{u}^* \right\rangle_g}{\Delta t}, \tag{2.43}$$

where p_g^{**} is the pressure at the second step of the pressure calculation and p_g^* is initially set to the value of p_g^n; subscript g means averaging over the gas phase. This equation is solved with the following Neumann boundary condition:

$$\left\langle \nabla \cdot \left(\frac{1}{\rho} \nabla p^{**} \right) \right\rangle_I = 0, \tag{2.44}$$

where the subscript I denotes an interphase averaging. The value of p_g^{**} is then given to p_g^* and Eqs. (2.43) and (2.44) are solved iteratively. Convergence is achieved when p^{**} is equal to p^*, and then this value initializes pressure p^{n+1} at the end of time step.

(b) Improvement of interface sharpness

When the surface tension is very small, a spurious numerical fragmentation of the interface was observed in gas-liquid two-phase flow simulations using the present particle method. To prevent this numerical inconvenience and maintain a sharp gas-liquid interface, we add, in accordance with the approach developed for the SPH method (Grenier et al., 2009), the following term to the right-hand side of the N-S equation:

$$\psi_i = \varepsilon \cdot \frac{S}{Vn^0} \cdot \sum_{phase(i) \neq phase(j), j \neq i} p_s \cdot \frac{\vec{r}_j - \vec{r}_i}{r_{ij}} \cdot w_{ij}, \tag{2.45}$$

where p_s is the pressure at the interface between particle i and j given by

$$p_s = p_i + \frac{p_j - p_i}{\left| \vec{r}_{ij} \right|} R. \tag{2.46}$$

Based on numerical experience, we set the adjustable parameter ε to 0.2 in the present study. We applied this interface sharpness model to simulate single bubble rising in the liquid pool and compared the simulation result (Figure 2.2-2, left) with the original

simulation result (Figure 2.2-2, right). The interface between liquid and gas was clearly sharpened using this model.

2.3 Summary

In this chapter, a computational framework was developed to simulate multi-phase flows based on particle methods. Surface tension model suitable for particle methods and the DEM were described. Two-step pressure algorithm and interface sharpness model were applied to enhance the stability of the FVP method when simulating multi-phase flows.

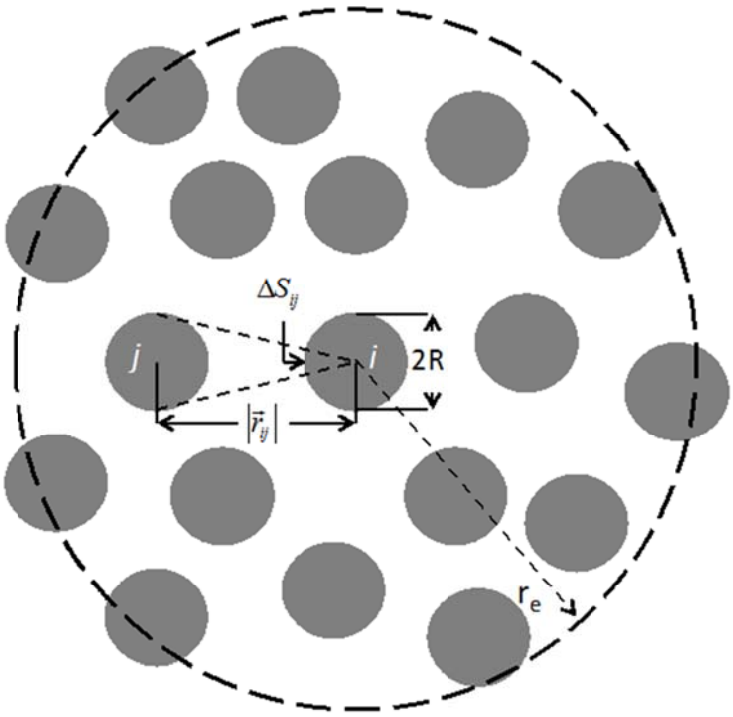

Figure 2.1-1. Neighbor particles of particle i in the cut-off radius

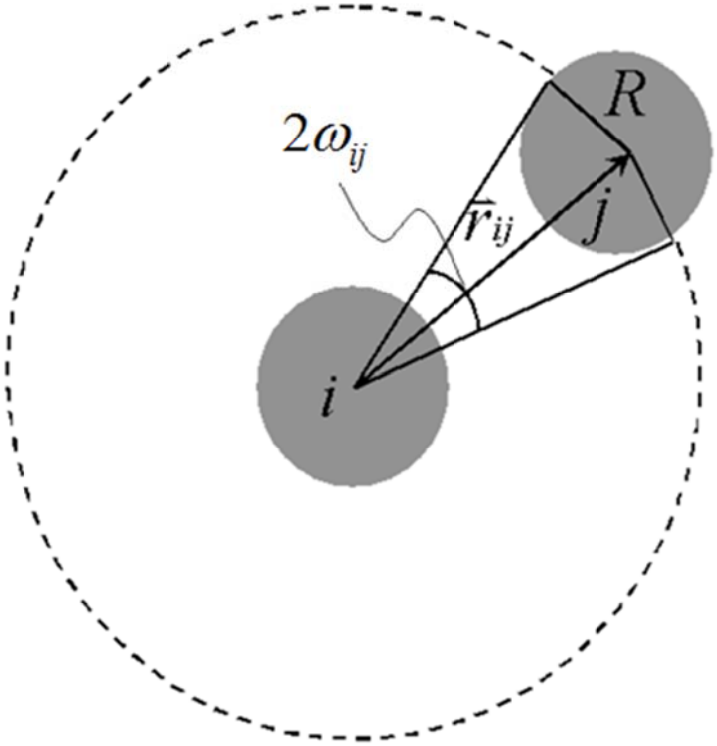

Figure 2.1-2. Two-dimensional interactions between finite volume particles.

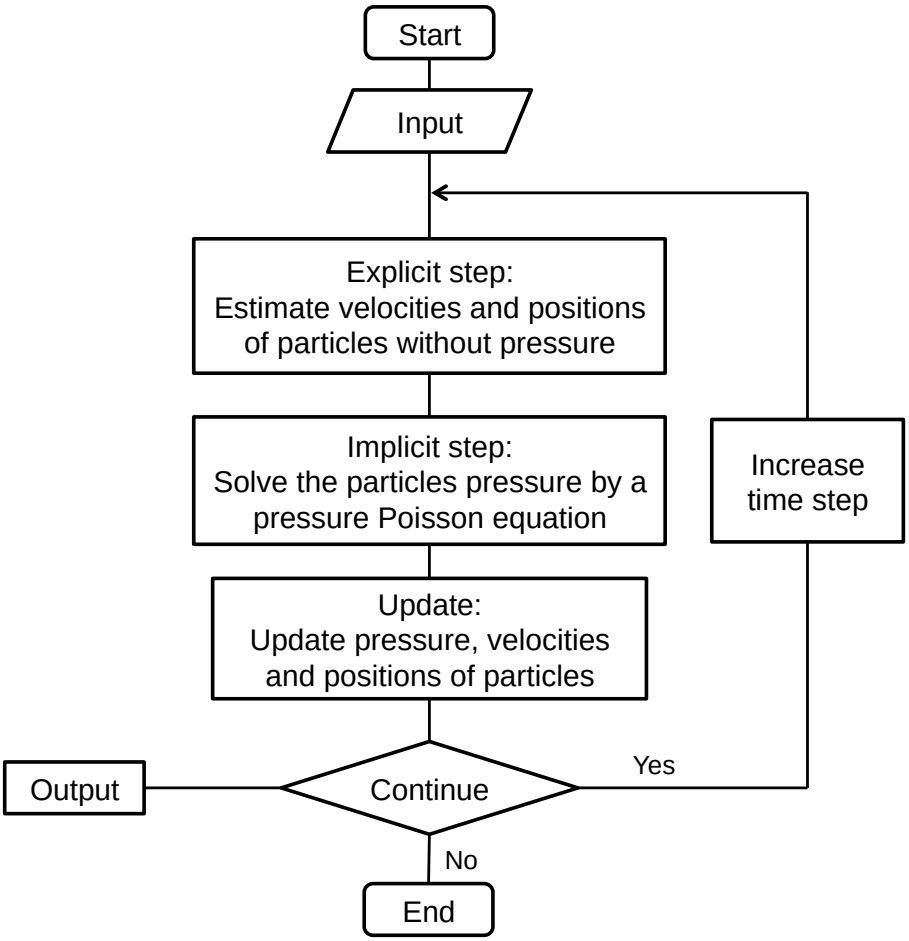

Figure 2.1-3. Explicit-implicit algorithms.

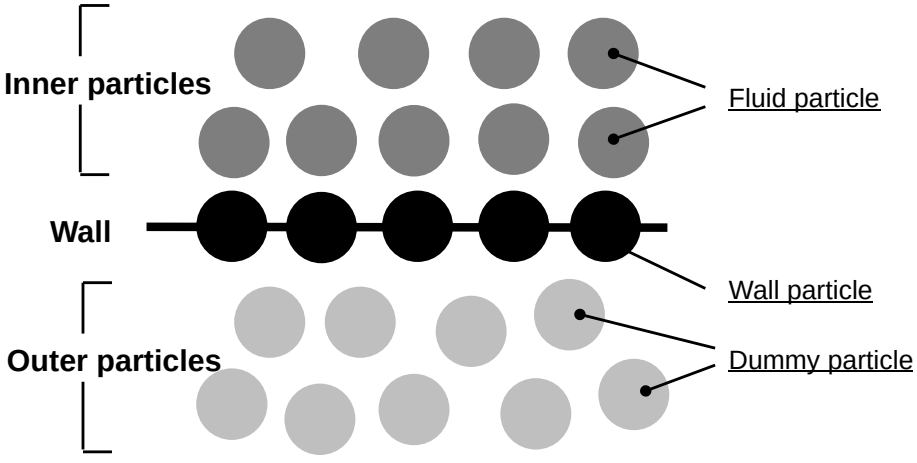

Figure 2.1-4. Wall boundary with dummy particles.

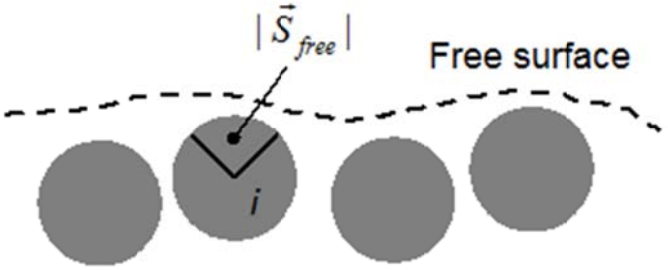

Figure 2.1-5. Free surface boundary.

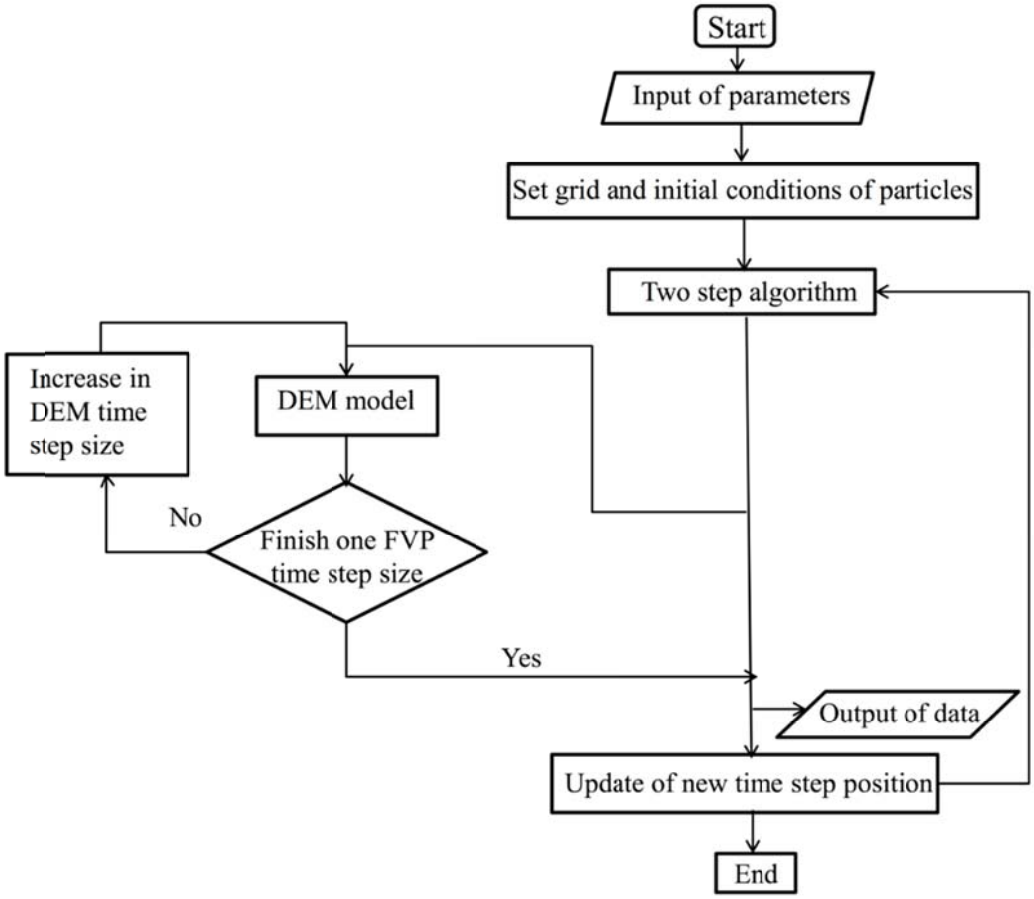

Figure 2.2-1. Numerical algorithm combining the FVP method and the DEM.

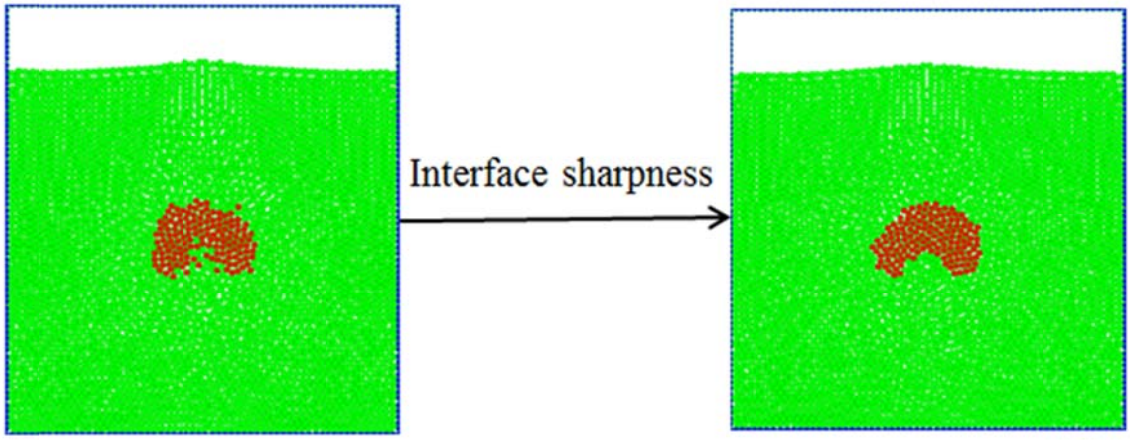

Figure 2.2-2. Simulation result of single bubble rising in liquid pool by applying the interface sharpness model.

Chapter 3

Multi-phase Flow Simulations Using Particle Method

In this chapter, behavior of single bubble rising in liquid pool is studied using the FVP method. Then three-phase (gas–liquid–solid) flow is simulated using the developed FVP method. Interactions due to contact and collision among solid particles (hereafter called particle-particle interactions) are modeled by the conventional DEM, and a modeling method based on the apparent viscosity model and the drag force model is investigated to simulate the particle-fluid interactions. Simulation results are compared with experiments of single bubble rising in a tank of stagnant solid particle-liquid mixture.

3.1 Introduction

The FVP method is very appropriate for multi-phase simulations because the interface is always clearly represented in calculations. The rise of bubbles in a liquid driven by a buoyancy force is a fundamental multi-phase phenomenon. A large number of numerical studies have addressed this problem. For example, a modified VOF method incorporating surface tension stresses in a 2D as well as 3D coordinate framework was investigated (Chen et al, 1999). In this modified VOF method, a semi-implicit algorithm on a non-staggered mesh is used to track the interface. Moreover, an interface-capturing method was developed and applied to single bubble problem with capillary effects (Bonometti and Magnaudet, 2006). This improved technique was developed to obtain a versatile tool for computing general 3D simulations with two- and three-phase flows involving high density and viscosity contrasts. An improved numerical algorithm based on the front tracking method was further extended to simulate 3D bubbles rising in

viscous liquids (Hua, 2008). In this work, the 3D bubble surface is tracked explicitly using an adaptive, unstructured triangular mesh, and the background mesh used a finite volume scheme. A Lattice Boltzmann method based on the phase-field method was also applied in the single bubble dynamics (Kurtoglu et al, 2006). On the other hand, with the development of the particle methods, they have been already applied to the bubble problems. Based on the MPS method, several hybrid methods were proposed for gas–liquid flows simulations (Yoon et al., 2001; Liu et al., 2005). In addition, another two-phase MPS (T-F MPS) method was developed for gas-liquid two-phase flows simulations and well represented several complicated two-phase flows phenomena (Shirakawa et al., 2001).

There has been successful simulation using particle methods of the interactions of a single solid body within a fluid. For example, the MPS method together with the passively moving solid (PMS) model has been used to simulate a solid floating in breaking waves (Koshizuka et al., 1998) and a ship profile being hit by a wave has been simulated using the particle finite element method (Idelsohn et al., 2006). These studies show that particle methods might assist in the direct simulation of fluid–solid mixture flows without interface tracking between phases. The FVP method was successfully coupled with DEM (Balevičius et al, 2008) and PMS model to simulate solid–fluid mixture flows (Zhang et al., 2009). A multi-time-step algorithm was introduced to efficiently combine the FVP calculation using the pressure implicit splitting of operators (PISO) algorithm (Issa et al., 1986) and the DEM calculation using a fully explicit algorithm that applies a relatively smaller time step size.

To further extend these particle-based simulations to solid particle-fluid mixture flows, appropriate modeling of the hydrodynamic interactions between solid particles and fluid (hereafter called particle-fluid interactions) might be necessary. There are two ways to

calculate the interactions. One is the apparent viscosity model of solid particle-fluid mixture, which describes the viscosity increase of liquid mixed with solid particles (Frankel and Acrivos, 1967). The other is the drag force model for particle-fluid interactions (Gidaspow, 1994; Ergun, 1952; Wen and Yu, 1966; Ding and Gidaspow, 1990).

3.2 Simulation of single bubble rising in liquid pool

To validate the present approach based on the FVP method extended to multi-phase flow systems, dynamics of various single bubbles rising in quiescent viscous liquids was simulated. The simulation results are compared with existing experimental data (Grace et al., 1976) on the terminal shape and rise velocity of bubbles. They are correlated in terms of three dimensionless numbers, that is the Eötvös number (Eo), the Morton number (M) and the bubble Reynolds number (Re). They are defined by

$$Eo = g\left(\rho_l - \rho_g\right)d^2 / \sigma , \tag{3.1}$$

$$M = g\mu_l^4\left(\rho_l - \rho_g\right)/\left(\rho_l^2\sigma^3\right), \tag{3.2}$$

$$Re = \rho_l V_t d / \mu_l , \tag{3.3}$$

where g denotes the gravitational acceleration, d the volume-equivalent bubble diameter and V_t the terminal velocity. Figure 3.2-1 shows what is called Grace's regime map, which provides the terminal shape and rise velocity of a gas bubble in viscous liquids.

The simulations using the developed code were performed for several important regimes given in the bubble diagram of Grace's map. In Table 3.2-1, the values of the selected Morton and Eötvös numbers are given for the present simulations of bubbles in the different regimes. The corresponding points in Grace's map are indicated in Figure 3.2-1.

Figure 3.2-2 shows the computational model used in the present simulations. The size of the computational domain is 12.0 cm and 12.8 cm in the lateral and axial direction, respectively. The center of the gas bubble with a diameter of 2.0 cm is initially located at

4.0 cm height from the bottom on the center axis of the domain. The initial distance between numerical particles is 0.8 mm. The total number of particles is 24,494, and 540 particles are used to represent the single gas bubble. The liquid/gas density and viscosity ratios are ρ_l / ρ_g = 1,000 and μ_l / μ_g = 100, respectively.

3.2.1 Bubble shapes

The results of calculated terminal bubble shapes are summarized in Figure 3.2-3. It can be seen that Case 1 corresponds to the spherical; Cases 2 ellipsoidal; Case 3 spherical-cap shapes; and Case 4 dimpled ellipsoid-cap. They agree well with the typical bubble shapes in Grace's map. The present simulation based on the FVP method provides reasonable solutions on bubble shape. It should be noted that it is difficult for the present FVP method to simulated skirted bubble shape due to drastic shape change of the bubble.

3.2.2 Bubble terminal velocity

In the present simulations, the rise velocity of a bubble is evaluated by

$$u_b = \frac{\sum_{i \in gas} u_i}{N}, \tag{3.4}$$

where u_i is the gas particle's velocity in the vertical direction, and N is the total number of gas particles.

The bubble Reynolds numbers, which is defined by Eq. (3.3), are calculated using a time-averaged rise velocity of bubble with terminal state. Table 3.2-2 compares the bubble Reynolds numbers between the simulation and experimental results. The later ones are experimental results obtained from the diagram of Grace's map. From this comparison, we can see that the two-step method can get closed results to experimental results. Slight underestimation has also been observed when simulating single bubble behavior using the FVP method coupled with CUP (Combined, Unified Procedure) algorithm (Zhang et al.,

2008). Generally the two-step method can reasonably simulate two-phase flows with a relatively large difference of the physical properties between phases.

3.3 Simulation of gas-liquid-solid three-phase flow

3.3.1 Rising bubble experiment

A fundamental experiment, the single bubble rising up in a tank of stagnant liquid was performed to verify the developed particle-based simulation code. Figure 3.3-1 shows a schematic of the experimental setup. A rectangular tank, with effective dimensions of 20 cm in height, 15 cm in width, and 4.5 cm in breadth, was made of transparent acrylic resin for visual observation and video recording. A single bubble was released near the bottom of the tank by bursting an air-filled rubber balloon with a pin. Its initial shape was approximately spherical with diameter of about 2.0 cm. Two fluids were used, a single-phase liquid and a solid particle-liquid mixture. Silicone oil and spherical glass particles were chosen as liquid and solid phases, respectively. This mixture aided viewing the bubble rising in the solid particle-liquid mixture because they have roughly the same refractive index of about 1.4. Diameters of the glass particles were within the range 0.85 mm–1.0 mm. The initial level of the tank fluid was 180 mm. The volume fraction of the glass particles mixed with the silicone oil was 49 %.

A high-speed camera was used to record the bubble rising. The tank was backlit to ensure high-quality recording. Photographic stills extracted from these recordings were used to measure the bubble's velocity and shape. Table 3.3-1 lists the physical properties of the gas, liquid, and solid phases used in the present experiment.

3.3.2 Simulation conditions

Numerical simulations of the rising bubble under the condition of the experiment were performed to validate the code for basic gas-liquid two-phase flows. The initial bubble

diameter was set to 20 mm; the initial distance Δl between adjacent particles was set to 0.9 mm, which corresponded to the diameter of the glass particles used in the experiment. The time step size was chosen as 1.0×10^{-5} s. The initial geometrical arrangement of numerical particles is the same as the experimental setup (Figure 3.3-1). The bubble was initially released about 40 mm above the bottom of the tank. In the three-phase flow calculations, liquid numerical particles were allocated randomly among solid particles in the tank giving the same mixture ratio as that in the experiment. Table 3.3-2 lists the physical properties of solid particles including the model parameters. Although the viscous damping coefficients are adjustable in the DEM calculations, their values, between 1 kg/s and 1,000 kg/s, were found to be largely immaterial in simulations. Here we set them to 10 kg/s.

3.3.3 Simulation results

(a) Single bubble rising in a liquid

Figure 3.3-2 presents a comparison of bubble shapes in stagnant liquid at times 0.05, 0.10, 0.15, and 0.20 s from experimental and simulation results. From experimental data, the bubble shape transformed gradually from an initial sphere to a dimpled ellipsoidal cap. This trend is well reproduced by the present simulation, although the simulated bubble shape is rather spherical in the early transient stage. The measured bubble velocities are compared with velocities from simulation (Figure 3.3-3). The bubble accelerates upward reaching a final terminal velocity at around 0.15 s. Simulated bubble velocities are smaller compared with experimental data during the early advance of the bubble. This might be caused by inconsistency in the initial bubble shape between simulation and experiment. In the experiments, the initial bubble shape was not perfectly spherical, but became slightly longer in height during the detachment of balloon rubber film. The longer bubble can be much accelerated because smaller drag to its surroundings in comparison with a spherical bubble as assumed in the present simulation. Nevertheless, the terminal velocity in

simulations and experiment, of about 0.19 m/s, are in good agreement. These results for a single bubble rising in a tank of stagnant liquid demonstrate the validity of the present particle-based simulation.

(b) Calculation with particle-particle interactions

Figures 3.3-4 and 3.3-5 show comparisons between experimental and simulation results of shape and velocity, respectively, of a bubble in a stagnant solid particle-liquid mixture. The original calculation, which did not consider the particle-particle interactions, poorly reproduces the observed bubble shape changes (see Figure 3.3-4). They are similar to those observed in the single-phase liquid. In contrast, the calculation using DEM, with particle-particle interactions included, produces better bubble shapes, which, although not dimpled ellipsoidal caps, are nevertheless slightly elongated laterally. From Figure 3.3-5, the bubble velocity is overestimated in both the original and the DEM calculations. The latter suggests that particle-particle interactions contribute to bubble dynamics, as represented by changes in bubble shape and bubble velocity in the solid particle-liquid mixture. However, we need further improvements in current simulations, especially for bubble velocity. Two additional models were tested to confirm the effect of particle-fluid interactions on the bubble behavior in a mixture.

(c) Empirical model for drag force between solid particles and fluid

The simulations discussed above did not model the particle-fluid interactions explicitly, and hence their effect on bubble dynamics was underestimated. We then introduced the drag force model in calculating particle-fluid interactions. The interaction force, denoted $\vec{f}$ is expressed by

$$\vec{f}_{fs} = \frac{\beta}{1-\alpha_g}(\vec{u}_p - \vec{u}_f), \tag{3.5}$$

where α_g is the void fraction, $\vec{u}_f$ the fluid velocity, and $\vec{u}_p$ the velocity of the solid particle. The momentum exchange coefficient β between solid particles and fluid was calculated using the conventional Gidaspow drag correlation (Gidaspow, 1994), which combines the Ergun equation (Ergun, 1952) and the Wen–Yu equation (Wen and Yu, 1966):

$$\beta = \begin{cases} 150\dfrac{(1-\alpha_g)^2}{\alpha_g}\dfrac{\mu_f}{d_p^2} + 1.75(1-\alpha_g)\dfrac{\rho_f}{d_p}\left|\vec{u}_f - \vec{u}_p\right| & \alpha_g \le 0.8 \\ \dfrac{3}{4}C_d\dfrac{\alpha_g(1-\alpha_g)}{d_p}\rho_f\left|\vec{u}_f - \vec{u}_p\right|\alpha_g^{-2.65} & \alpha_g > 0.8 \end{cases}, \quad (3.6)$$

where d_p is the diameter of solid particle, and C_d the drag coefficient given as a function of Reynolds number Re_p of the particle (Ding et al., 1990):

$$C_d = \begin{cases} \dfrac{24}{Re_p}(1 + 0.15Re_p^{\,0.687}) & Re_p \le 1000 \\ 0.44 & Re_p > 1000 \end{cases}, \quad (3.7)$$

$$Re_p = \frac{\left|\vec{u}_f - \vec{u}_p\right|\alpha_g\rho_f d_p}{\mu_f}. \quad (3.8)$$

From Eq. (3.6), β is discontinuous at α_g = 0.8, and hence a smoothing function (Ding et al., 1990) was applied. The particle-fluid interaction force based on the Gidaspow drag correlation is dependent not only on the relative velocity between fluid and solid but also on the presence of other surrounding particles. In Eq. (3.5) the velocity $\vec{u}_p$ of solid particles around the fluid particle i is calculated as

$$\vec{u}_p = \frac{\sum_{j\in solid,neigh(i)} \omega_{ij}\vec{u}_j}{\sum_{j\in solid,neigh(i)} \omega_{ij}}, \quad (3.9)$$

where the summations are performed only for neighboring solid particles and the weight function is given by

$$\omega_{ij} = \frac{r_e}{r_{ij}} - 1.0 \,. \tag{3.10}$$

Here r_e was set to $4.1\,\Delta l$ used in the present two-dimensional simulations. From numerical tests, it was found that results have little sensitivity to the choice of r_e in the present simulations.

The simulation and experimental results for shape and velocity of the bubble are compared in Figures 3.3-6 and 3.3-7, respectively. A comparison of the bubble shapes with time-lapse photos and velocity with experimental data is given in Figures 3.3-6 (top row) and 3.3-7 (solid dots), respectively. One simulation considered only particle-fluid interactions based on the Gidaspow drag correlation; the other included using DEM. Clearly, shape and velocity are quite different from the experimental results. Note that in the simulations the shape and velocity are not obtained after the bubble reaches the surface of the pool. In contrast, the simulation with both particle-fluid and particle-particle interactions predicts more reasonable bubble velocities in the first 0.4 s compared with those from experiment. However, afterwards, the bubble shape becomes distorted and bubble velocities increase rapidly. From the present two simulations, it is found that not only the particle-particle but also particle-fluid interactions are of considerable importance in bubble shape development and changes in velocity.

(d) Theoretical model for apparent viscosity of particle-fluid mixture

In general, particle-liquid mixtures with high solid fraction should have rather large apparent viscosity owing to hydrodynamic interactions between neighboring particles. To consider its effect on bubble behavior, the liquid viscosity was replaced by the effective one based on the following Frankel–Acrivos expression theoretical equation (Frankel and Acrivos, 1967):

$$\frac{\mu_{eff}}{\mu_0} = \frac{9}{8}\frac{(\alpha_p / \alpha_{\max})^{1/3}}{1-(\alpha_p / \alpha_{\max})^{1/3}}, \tag{3.11}$$

where μ_{eff} is the apparent viscosity of the solid particle-fluid mixture, μ_0 the liquid viscosity, α_p the volume fraction of solid particles in the mixture, and $\alpha_{\max}$ the maximum volume fraction of solid particles in the mixture. Here α_p is calculated as

$$\alpha_p = \frac{Num_s}{Num_s + Num_l + Num_g}, \tag{3.12}$$

where Num_s, Num_l and Num_g are the numbers of numerical particles in solid, liquid and gas phases, respectively, within the controlling region with a radius of $4.1\Delta l$ used in the present simulations. Simulation results were not sensitive to the size of the controlling region. Eq. (3.11) developed for a concentrated suspension of spherical particles can predict the rapid rise of the viscosity, which is observed at high concentrations. For the particle-fluid mixture used, $\frac{\mu_{eff}}{\mu_0}$ is evaluated as 12.3.

Figures 3.3-8 and 3.3-9 present comparisons between experimental and simulation results of bubble shape and velocity, respectively. A comparison of the bubble shapes with time-lapse photos and velocity with experimental data is given in Figures 3.3-8 (top row) and 3.3-9 (solid dots), respectively. Here, the two simulations considered the particle-fluid interactions with apparent viscosity based on Eq. (3.11), and additionally the particle-particle interactions using DEM. Bubble shapes obtained in simulations using only the apparent viscosity reproduce satisfactorily the ellipsoidal shape at 0.4 s. However, in this simulation, the bubble velocity is overestimated. The other simulation using both the apparent viscosity model and DEM predicts a more reasonable bubble velocity. Although in simulations the bubble shape is slightly longer in height than that in the experiment

during the early stage, it approaches the observed shape at 0.8 s. The discrepancy, especially in the early transient stage, may be caused by conditions on bubble release.

3.4 Discussion

The present particle-based simulations indicate that, on the whole, the calculation with the apparent viscosity of solid particle-fluid mixture can reasonably reproduce the observed bubble dynamics in the experiments conducted, as indicated by the changes in bubble shape and velocity. However, the apparent viscosity model based on the Frankel–Acrivos expression is formulated to describe hydrodynamic interactions of neighboring spheres as a function of the volume fraction of solid particles only. It is unclear whether it is generally applicable to other multiphase flow conditions that depend on various particle sizes and involve relative velocities between solid and fluid phases.

The calculation, taking into account particle-fluid interactions based on the Gidaspow drag correlation as well as particle-particle interactions using DEM, did not necessarily present reasonable results in comparison with measured bubble characteristics. In general, empirical drag correlations are developed as a function of physical variables, which represent bulk flow properties. Therefore, it is necessary to check its applicability to particle-based simulations, which model meso-scale behaviors of multi-phase flows.

In the present simulations, all the cases were calculated in a two dimensional system. The effect of the front and back walls of the tank on the rising bubble cannot be considered in the present 2D simulations. In gas-liquid two-phase simulation, both the bubble shape and velocity were in reasonable agreement with the experimental data generally, and hence that their effect might not be dominant on the rising bubble motion in the experiment. In the case of particle-fluid mixture simulation, the apparent viscosity of the mixture is quite large and the movement of the particle-liquid mixture is very slow. As a result, the existence of

the walls would not change the rising bubble motion. Nevertheless, three-dimensional calculation is necessary to model the actual bubble shape in the pool for more reasonable simulation of drag acting on the bubble.

3.5 Summary

To develop a computational framework for multi-phase flow simulations, a single bubble rising in a stagnant liquid and solid particle-liquid mixture were simulated using a two-dimensional particle-based simulation code based on the FVP method. The gas-liquid two phase numerical simulations showed good agreement with experimental results. Gas-liquid-solid three phase numerical simulations, which considered the effects of solid particles, showed that interactions between solid particles and fluid as well as among solid particles contribute significantly to bubble behavior in the solid particle-liquid mixture. The calculation considering the apparent viscosity of a solid particle-fluid mixture, which is attributed to solid particle-fluid interactions, reproduced reasonable changes in bubble shape change and rise velocity in comparison with the measured data. Although further investigation is necessary to develop more appropriate constitutive models, the present study demonstrates a developed computational framework useful for numerical simulations of bubble dynamics in a solid particle-liquid mixture.

Table 3.2-1. Morton (M) and Eötvös (Eo) numbers for simulations of bubbles in different regimes.

Case	Eötvös number	Morton number
1	8.67	711
2	10	1.0×10^{-2}
3	32.2	8.2×10^{-4}
4	116	1.31

Table 3.2-2. Bubble Reynolds number for terminal rise velocities.

Case	1	2	3	4
Sim.	0.066	10.6	47.5	17.9
Exp.	0.078	11.0	55.3	20.4

Table 3.3-1. Physical properties of the gas, liquid and solid phases used in the bubble experiment.

	Gas	Liquid	Solid
Material	air	silicone oil	glass
Density ρ	1.205 kg/m^3	1,070 kg/m^3	2,200 kg/m^3
Dynamic viscosity μ	1.822×10^{-5} Pa·s	0.482 Pa·s	---
Surface tension coefficient σ	---	2.52×10^{-2} N/m	---

Table 3.3-2. Physical properties of solid particles used in the DEM calculations.

Poisson's ratio, υ	0.25
Elastic modulus, E	7.50×10^{10} Pa
Shear modulus, G	2.92×10^{10} Pa
Friction coefficient, η	0.4
Viscous damping coefficients	
Normal direction, γ_n	10.0 kg/s
Tangential direction, γ_t	10.0 kg/s

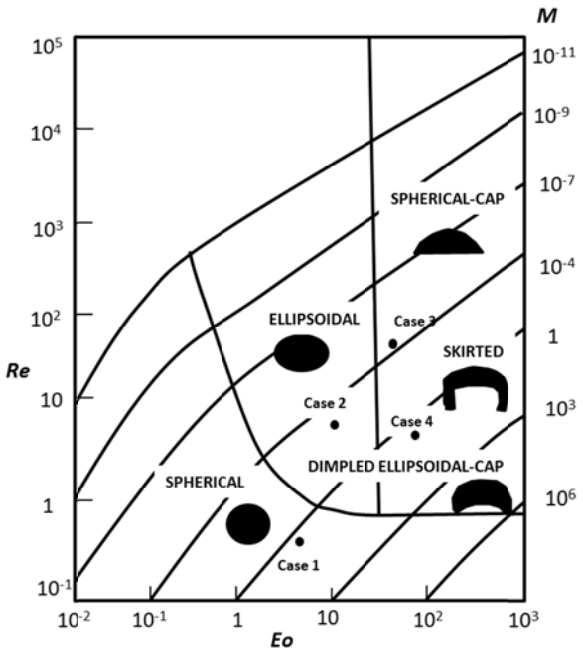

Figure 3.2-1. Bubble diagram for the shape and terminal rise velocity of gas bubbles in quiescent viscous liquids (Grace's regime map).

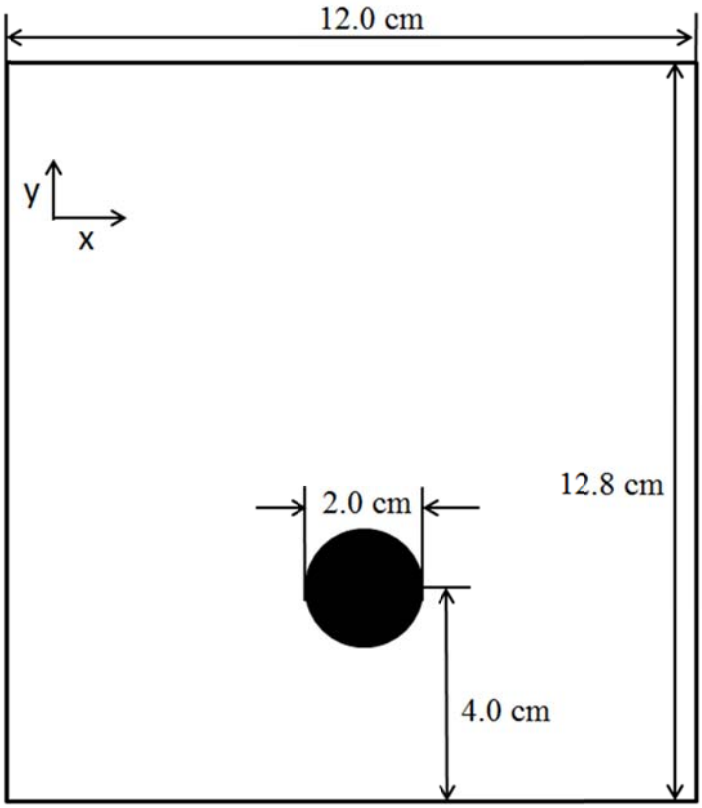

Figure 3.2-2. Initial condition for single bubble simulations.

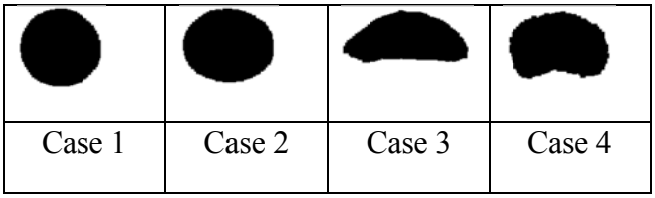

Figure 3.2-3. Simulated terminal bubble shapes.

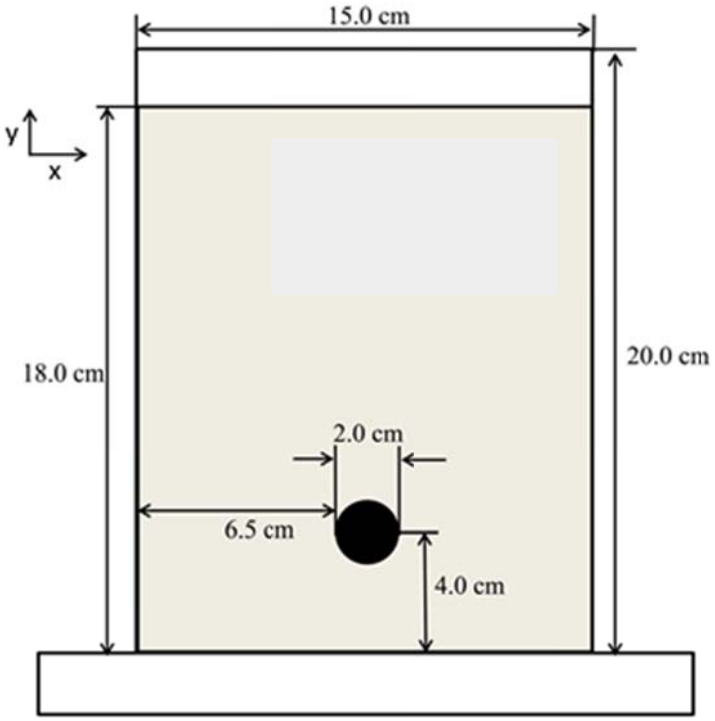

Figure 3.3-1. Schematic of the rising bubble experiment.

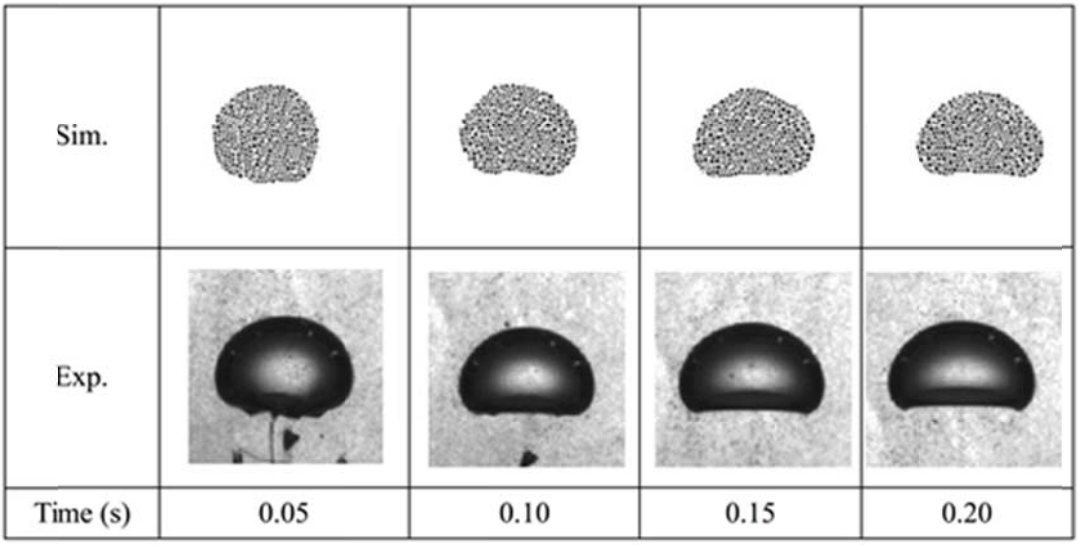

Figure 3.3-2. Comparison between simulation and experiment of shape of a bubble in liquid.

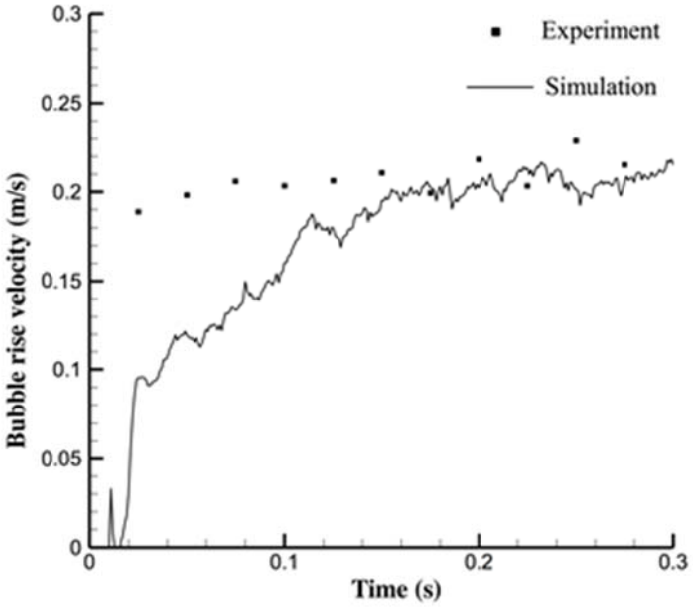

Figure 3.3-3. Comparison between simulation and experiment of velocity of a bubble in liquid.

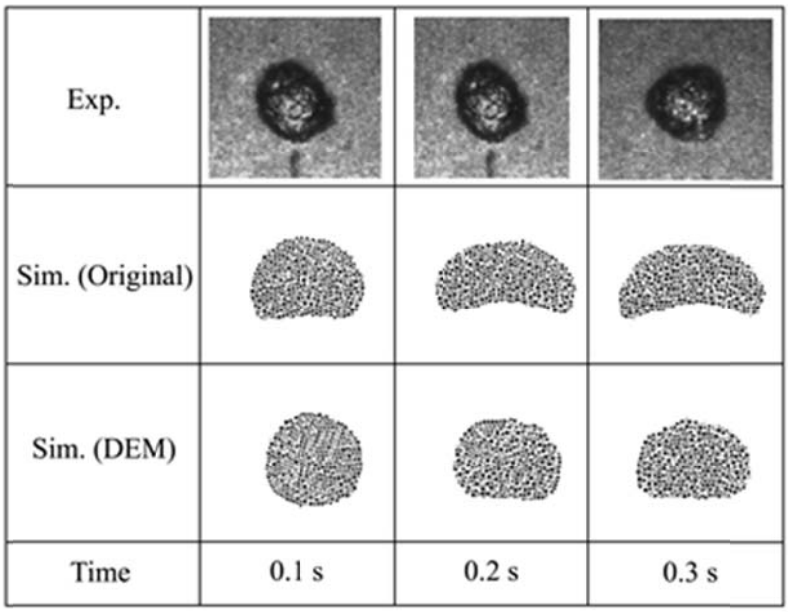

Figure 3.3-4. Effect of particle-particle interactions on shape in simulations of a bubble in a particle-liquid mixture.

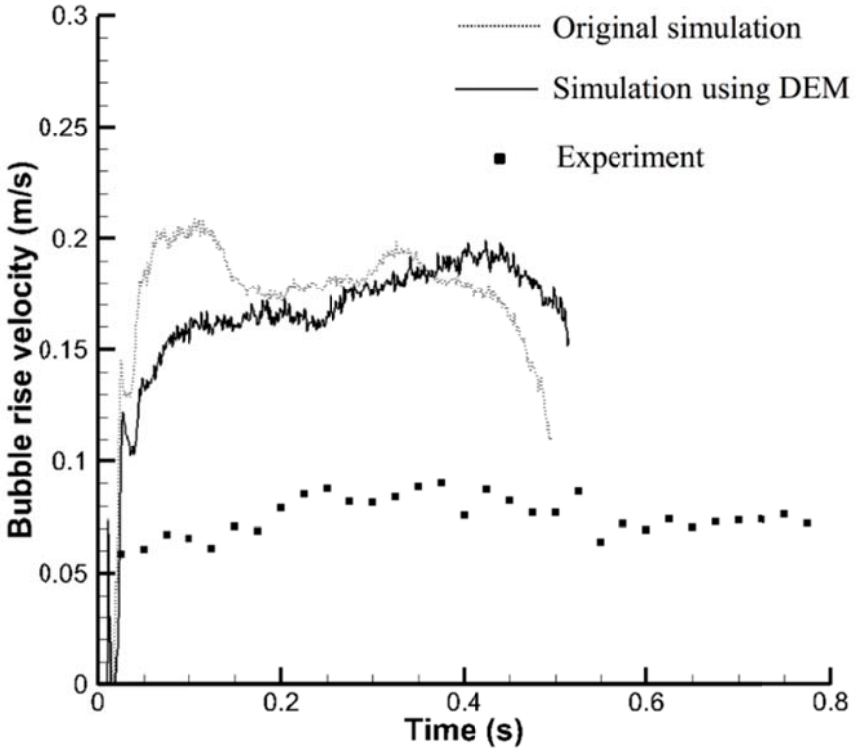

Figure 3.3-5. Effect of particle-particle interactions on velocity in simulations of a bubble in particle-liquid mixture.

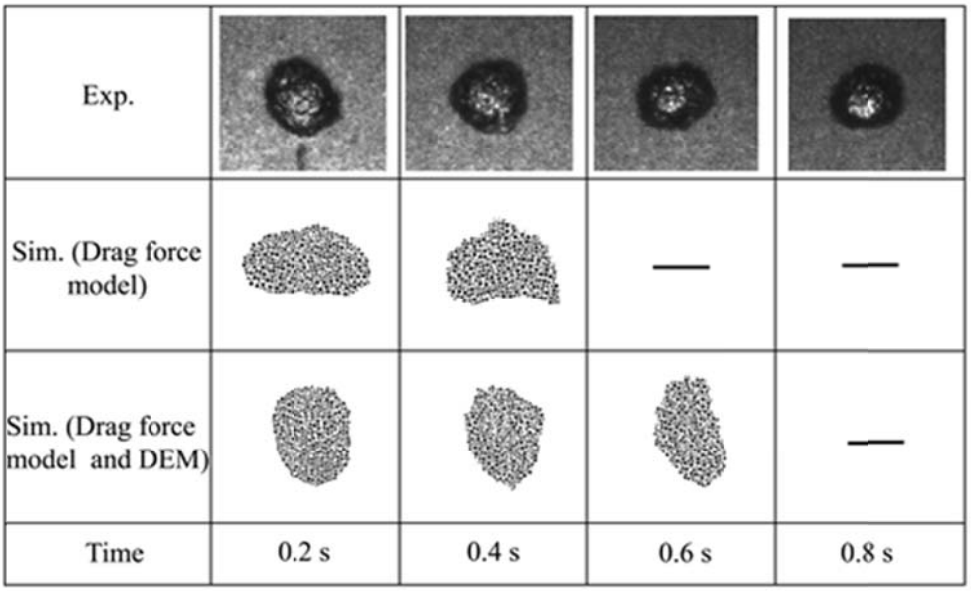

Figure 3.3-6. Effect of particle-fluid interactions on bubble shape in solid particle-fluid mixture from simulations (particle-fluid interactions are taken into account using the empirical model for drag force).

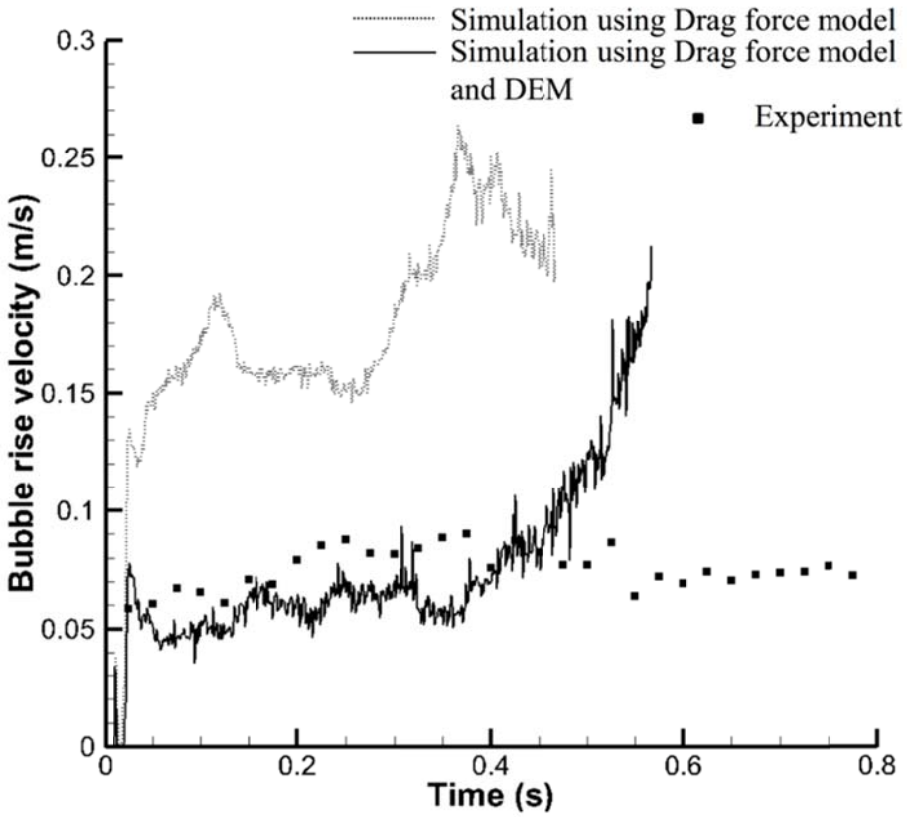

Figure 3.3-7. Effect of particle-fluid interactions on bubble velocity in particle-fluid mixture in simulations (particle-fluid interactions are taken into account using the empirical model for drag force).

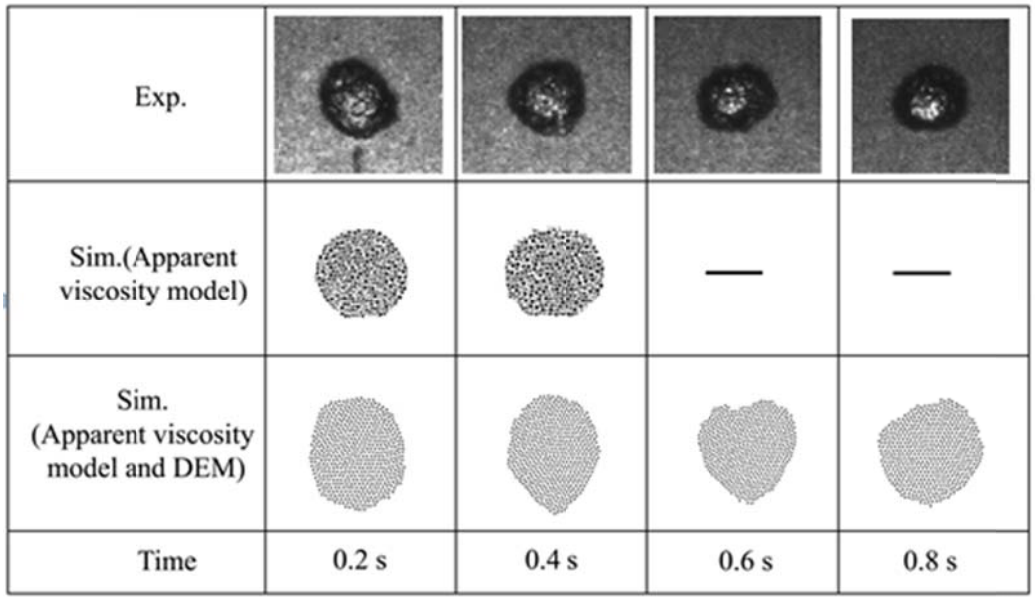

Figure 3.3-8. Effect of particle-fluid interactions on shape for a bubble in a particle-fluid mixture from simulations (particle-fluid interactions are calculated using the theoretical model for apparent viscosity).

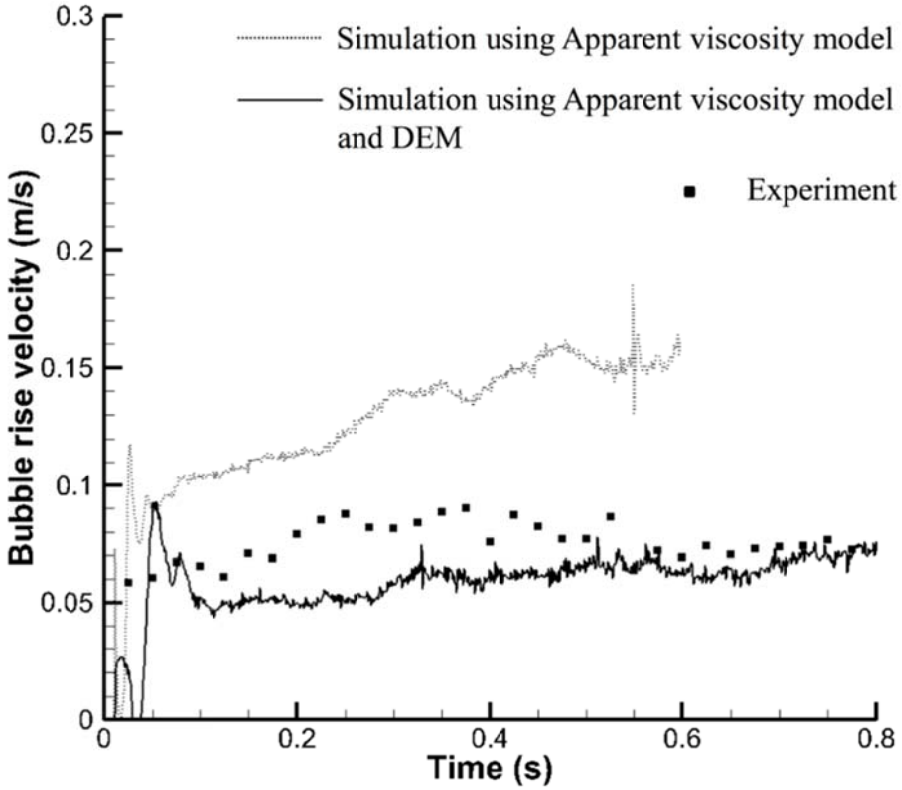

Figure 3.3-9. Effect of particle-fluid interactions on bubble velocity in particle-fluid mixture from simulations (particle-fluid interactions are calculated using a theoretical model for apparent viscosity).

Chapter 4

Development of a Mesh-Particle Hybrid Method

Moving particle methods can easily capture the interface when simulating multi-phase flow, but calculation costs are much heavier compared with conventional grid methods and they may cause unphysical numerical oscillation of pressure with high frequencies. Typically, Eulerian-fixed grid methods, such as VOF, level set method and CIP method, possess the advantage of allowing stable pressure calculation, but making the calculation of the interface inaccurate.

A hybrid Eulerian–Lagrangian method, where the advection of fluid phase is handled in a Lagrangian manner while fluid velocity and pressure information is constructed on a fixed Eulerian grid, makes use of both approaches. So we want to develop a mesh-particle hybrid method which can capture the interface easily while the computation cost will not increase dramatically.

In this chapter, a mesh-particle hybrid method is developed for efficient and accurate simulations of two-phase flows. In this method, the main component of the flow is solved using the CIP/MM FVM; the two-phase interface is rendered using the FVP method. The effect of surface tension is evaluated using the continuum surface force model. Numerical particles in the FVP method are distributed only on the surface of the liquid in simulating the interface between liquid and gas; these particles are used to determine fluid density of each mesh grid. An artificial term is also introduced to mitigate particle clustering in the direction of maximum compression and sparse discretization errors in the stretched direction.

Then the mesh-particle hybrid method is developed to calculate incompressible, two-phase flows with phase change. Particles on the interface are used to calculate heat transfer and phase change.

Coupled with the CUP algorithm, the hybrid method is also extended to calculate compressible and incompressible flow simultaneously.

4.1 Overview of the CIP/MM FVM

The CIP/MM FVM (Xiao F, 2004) can be described using the 2D transport equation,

$$\frac{\partial \phi}{\partial t}+\frac{\partial}{\partial x}(u\phi)+\frac{\partial}{\partial y}(u\phi)=0\,, \tag{4.1}$$

where ϕ is the transported quantity. Both the VIA and the SIA are defined respectively for the physical variable $\phi(x,y,t)$ as ${}^{V}\phi$ and ${}^{S^x}\phi$. A 2D control volume is shown in Figure 4.1-1. VIA is defined on the volume elements V_{ij} and SIAs are defined on the surface elements ($S^x_{i\pm1/2,j}$ $S^y_{i,j\pm1/2}$). The expression of VIA over each mesh cell is given by

$${}^{V}\phi_{ij}(t)=\frac{1}{|V_{ij}|}\int_{x_{i-1/2}}^{x_{i+1/2}}\int_{y_{i-1/2}}^{y_{i+1/2}}\phi(x,y,t)dxdy\,. \tag{4.2}$$

At the cell boundaries, SIAs are calculated using

$${}^{S^x}\phi_{i+1/2,j}(t)=\frac{1}{S^x_{i+1/2,j}}\int_{y_{j-1/2}}^{y_{j+1/2}}\phi(x_{i+1/2},y,t)dy\,, \tag{4.3}$$

$${}^{S^y}\phi_{i,j+1/2}(t)=\frac{1}{S^y_{i,j+1/2}}\int_{x_{i-1/2}}^{x_{i+1/2}}\phi(x,y_{j+1/2},t)dx\,. \tag{4.4}$$

Here, the volume $|V_{ij}|$ is given by $|V_{ij}|=\Delta x_i\Delta y_j$; $S^x_{i+1/2,j}$ and $S^y_{i,j+1/2}$ are the side lengths of the surface element, which are defined as $S^x_{i+1/2,j}=\Delta y_i$ and $S^y_{i,j+1/2}=\Delta x_i$, respectively.

The CIP-CSL3 scheme (Yabe et al., 2001) used handling the advection computation, is based on a cubic interpolation function constructed from both VIA and SIA of the

transported quantity. In the x direction, taking the case of $u<0$, a left-bias interpolation can be written as

$$\phi_i^L(x)=a_3(x-x_{i-1/2})^3+a_2(x-x_{i-1/2})^2+a_1(x-x_{i-1/2})+a_0. \tag{4.5}$$

The parameters, a_0, a_1, a_2, and a_3, in this cubic interpolation function can be determined using the following constrained conditions:

$$\phi_i^L(x_{i-1/2})={}^{S_x}\phi_{i-1/2,j}, \tag{4.6}$$

$$\phi_i^L(x_{i+1/2})={}^{S_x}\phi_{i+1/2,j}, \tag{4.7}$$

$$\frac{1}{\Delta x}\int_{x_{i-1/2}}^{x_{i+1/2}}\phi_i^L(x)dx={}^{V}\phi_{i,j}, \tag{4.8}$$

$$\frac{d\phi_i^L}{dx}|_{x=x_i}=\chi_i, \tag{4.9}$$

where χ_i is the slope of the interpolation function at the cell center.

In terms of ${}^{S_x}\phi_{i-1/2,j}$, ${}^{S_x}\phi_{i+1/2,j}$, ${}^{V}\phi_{i,j}$ and χ_i, the polynomial can be completely determined with , and the coefficients read

$$a_1=-\frac{6}{\Delta x_i}{}^{V}\phi_{i,j}+\frac{6}{\Delta x_i}{}^{S_x}\phi_{i+1/2,j}-2\chi_i, \tag{4.10}$$

$$a_2=-\frac{6}{\Delta x_i^{\,2}}{}^{V}\phi_{i,j}+\frac{3}{\Delta x_i}({}^{3S_x}\phi_{i+1/2,j}-{}^{S_x}\phi_{i-1/2,j})-\frac{6}{\Delta x_i}\chi_i, \tag{4.11}$$

$$a_3=\frac{4}{\Delta x_i^{\,3}}({}^{S_x}\phi_{i+1/2,j}-{}^{S_x}\phi_{i-1/2,j})-\frac{4}{\Delta x_i^{\,2}}\chi_i. \tag{4.12}$$

Analogously, the right-bias interpolation function in the following form

$$\phi_i^R(x)=a_3(x-x_{i+1/2})^3+a_2(x-x_{i+1/2})^2+a_1(x-x_{i+1/2})+a_0, \tag{4.13}$$

can also be derived from the same constraint conditions.

Once the interpolation function is determined, the SIA ${}^{S_x}\phi$ at time step n+1 is firstly updated by a semi Lagrangian solution as

$$ {}^{S_x}\phi^{*}_{i+1/2,j} = \begin{cases} \phi^{R}_{i,j}(x_{i+1/2}+\alpha) & if\ \alpha < 0 \\ \phi^{L}_{i+1,j}(x_{i+1/2}+\alpha) & if\ \alpha > 0 \end{cases}, \tag{4.14} $$

and then corrected according to the divergence of the velocity field

$$ {}^{S_x}\phi^{n+1}_{i+1/2,j} = {}^{S_x}\phi^{*}_{i+1/2,j} - \int_{\tau}(\phi\frac{\partial u}{\partial x})d\tau`, \tag{4.15} $$

where τ is the trajectory through which the semi-Lagrangian particle travels during Δt. The following approximation is used

$$ \int_{\tau}(\phi\frac{\partial u}{\partial x})d\tau` = \begin{cases} 0.5\,{}^{S_x}\phi^{*}_{i+1/2,j}({}^{S_x}u^{*}_{i+1/2,j} - {}^{S_x}u^{*}_{i-1/2,j} + {}^{S_x}u^{n}_{i+1/2,j} - {}^{S_x}u^{n}_{i-1/2,j})\Delta t/\Delta x_i \\ 0.5\,{}^{S_x}\phi^{*}_{i+1/2,j}({}^{S_x}u^{*}_{i+3/2,j} - {}^{S_x}u^{*}_{i+1/2,j} + {}^{S_x}u^{n}_{i+3/2,j} - {}^{S_x}u^{n}_{i+1/2,j})\Delta t/\Delta x_i \end{cases}, \tag{4.16} $$

where u^{*} is the provisional value of the velocity right after the semi-Lagrangian solution in fluid computation. The displacement is estimated by a Taylor approximation up to the third order as

$$ \alpha = -u_{i+1/2,j}\Delta t + \frac{1}{2}u_{i+1/2,j}(\Delta t)^2(\frac{\partial u}{\partial z})_{i+1/2} - \frac{1}{6}u_{i+1/2,j}(\Delta t)^3\left[(\frac{\partial u}{\partial z})_{i+1/2}{}^2 + u_{i+1/2,j}(\frac{\partial^2 u}{\partial z^2})_{i+1/2}\right], \tag{4.17} $$

where $(\frac{\partial u}{\partial z})_{i+1/2}$ and $(\frac{\partial^2 u}{\partial z^2})_{i+1/2}$ are computed by central differencing.

The VIA is advanced by a flux form from the conservative relation

$$ {}^{V}\phi^{n+1}_{i,j} = {}^{V}\phi^{n}_{i,j} - (\mathrm{g}_{i+1/2} - \mathrm{g}_{i-/2})/\Delta x_i, \tag{4.18} $$

where $\mathrm{g}_{i+1/2}$ represents the flux across boundary $x = x_{i+1/2}$ during $t^{n+1} - t^{n}$ and is computed as

$$ \mathrm{g}_{i+1/2} = \int_{x_{i+1/2}+\alpha}^{x_{i+1/2}} \phi^{R}_{i}(x)dx, \tag{4.19} $$

$$ \mathrm{g}_{i+1/2} = -\int_{x_{i+1/2}}^{x_{i+1/2}+\alpha} \phi^{L}_{i+1}(x)dx. \tag{4.20} $$

The SIA value is at first updated by a semi-Lagrangian step and then corrected by an extra step that evaluates the divergence term along the trajectory that semi-Lagrangian

particle travels during Δt. The VIA value is then computed by a flux-based formulation. The corresponding value in the y direction can similarly be updated.

4.2 Coupling of particle and mesh methods

4.2.1 Solution algorithm

In this hybrid method, computational solutions are first obtained on a staged mesh using the CIP/MM FVM. The governing equations are the followings:

$$\frac{\partial \rho}{\partial t} + \nabla \cdot \vec{m} = 0, \tag{4.21}$$

$$\frac{\partial \vec{m}}{\partial t} + \nabla \cdot (\vec{m} \otimes \vec{u}) = -\nabla p + f, \tag{4.22}$$

$$\frac{\partial \theta}{\partial t} + \nabla \cdot (\theta \vec{u}) = 0, \tag{4.23}$$

where $\vec{u}$ is the velocity, $\vec{m}$ the momentum, γ the specific heat ratio, and θ the color function. Value of θ ranges from 0 to 1. Here, a fractional step procedure is used. The terms in Eqs. (4.21)–(4.23) are split into advection and nonadvection components. First, the advection equations,

$$\frac{\partial \rho}{\partial t} + \nabla \cdot \vec{m} = 0, \tag{4.24}$$

$$\frac{\partial \vec{m}}{\partial t} + \nabla \cdot (\vec{m} \otimes \vec{u}) = 0, \tag{4.25}$$

$$\frac{\partial \theta}{\partial t} + \nabla \cdot (\theta \vec{u}) = 0, \tag{4.26}$$

are solved using the CIP-CSL3 scheme. With the nonadvection equation, the pressure-based projection is performed by solving the following Poisson equation for pressure,

$$\nabla^2 p^{n+1} = \frac{1}{\Delta t}(-\vec{u}^* \cdot \nabla \rho^{n+1} + \nabla \cdot \vec{m}^*), \tag{4.27}$$

where p^{n+1} is the iterated pressure of the next step, $\vec{u}^*$ the temporal velocity after advection, ρ^{n+1} the density at the next step, p^* the temporal pressure after advection and $\vec{m}^*$ is the temporal momentum after advection. We can then obtain the updated physical variables for each cell and go to the next step.

In the present hybrid method, particles are only distributed over the surface of the liquid (Figure 4.2-1). Particle insertion and deletion is permissible in accordance with flow conditions within the liquid.

The velocity of a particle is estimated by interpolating velocities at the cell centers of the fixed mesh grids around the particle, as illustrated in Figure 4.2-2. Next the particle is relocated given the iterated position

$$\vec{r}_i^{\,*} = \vec{r}_i^{\,n} + \vec{v}_i^{\,n}\Delta t\,. \tag{4.28}$$

We then use the FVP method to adjust the distribution of particles. The continuity equation requires that the divergence field for the fluid velocity should be zero:

$$\nabla\cdot(\vec{v}_i^{\,n} + \vec{v}_i^{\,'}) = 0\,. \tag{4.29}$$

The corrected value for the velocity is derived from the gradient of the corrected pressure p',

$$\vec{v}_i^{\,'} = -\frac{\Delta t}{\rho_i}\nabla p'\,, \tag{4.30}$$

where ρ_i is the density of fluid represented by particle i. Using Eqs. (4.28)–(4.30), the following Poisson equation for corrected pressure is obtained:

$$\frac{\Delta t}{\rho_i} < \nabla^2 p' >_i = \nabla\cdot\vec{v}_i^{\,'}\,. \tag{4.31}$$

This equation is discretized by the gradient and Laplacian models given in the FVP method and then solved by the incomplete Cholesky conjugate gradient (ICCG) algorithm with a Dirichlet boundary condition.

An artificial term was also introduced to avoid particle clustering in the direction of maximum compression and sparse discretization error in the stretching direction (Xu et al., 2009). The position of particle i is modified using the corrected velocity calculated from Eq. (4.30),

$$\vec{r}_i^{\,n+1} = \vec{r}_i^{\,*} + \vec{v}_i^{\,'}\Delta t + \delta\vec{r}_i\,, \tag{4.32}$$

where $\delta\vec{r}_i$ is the position correction vector of particle i defined as

$$\delta\vec{r}_i = \varepsilon\iota\vec{R}_i\,, \tag{4.33}$$

with ε a constant parameter, set to 0.01 in this study and ι a shifting magnitude equal to the maximum particle convection distance $U_{\max}dt$ given by the product of the maximum particle velocity $U_{\max}$ and time step size dt. The shifting vector $\vec{R}_i$ is defined by

$$\vec{R}_i = \sum_{j=1}^{N_i} \frac{\overline{r}_i}{r_{ij}^2}\vec{n}_{ij}\,, \tag{4.34}$$

where N_i is the number of neighboring particles around particle i and r_{ij} the distance between particles i and j. The average particle spacing $\overline{r}_i$ in the neighborhood of i is calculated using

$$\overline{r}_i = \frac{1}{N_i}\sum_{j=1}^{N_i} r_{ij}\,. \tag{4.35}$$

After shifting the particle positions, the density $\rho(i,j)$ of the grid (i,j) on the interface of liquid is calculated from

$$\rho(i,j) = \frac{N(i,j)}{N_0}\,, \tag{4.36}$$

where the numerical density of the grid is

$$N(i,j) = \sum_{d_{i,j,\alpha}<r_e} \omega_{ij\alpha}\,, \tag{4.37}$$

given weight functions $\omega_{ij\alpha}$

$$\omega_{ij\alpha} = \begin{cases} \dfrac{r_e}{d_{i,j,\alpha}} - 1 & d_{i,j,\alpha} < r_e \\ 0 & d_{i,j,\alpha} > r_e \end{cases}, \tag{4.38}$$

with r_e the control radius and $d_{i,j,\alpha}$ the distance between particle α and the center of grid (i, j).

Figure 4.2-3 presents the flow diagram of the numerical solution algorithm used in the present study.

4.2.2 Surface tension model in the hybrid method

In the present method, surface tension is modeled as a volume force using the CSF model (Brackbill et al., 1992) on mesh. In the CSF model, the surface tension force acts via a source term $\vec{F}_\sigma$ which only acts in the vicinity of the interface. $\vec{F}_\sigma$ is included in f in Eq. (4.22) as other forces. The expression for $\vec{F}_\sigma$ is given by

$$\vec{F}_\sigma = \sigma\kappa\vec{n}, \tag{4.39}$$

where $\vec{n}$ is the unit normal vector on the interface and κ is the curvature. $\vec{n}$ is calculated from the color function

$$\vec{n} = \frac{\nabla\theta}{|\theta|}, \tag{4.40}$$

κ is obtained from the divergence of the unit normal vector to the interface:

$$\kappa = \nabla\cdot(\vec{n}). \tag{4.41}$$

4.2.3 Heat transfer model

Heat transfer with melting has been studied extensively because of its great importance in many industrial applications. Typically, numerical methods for solving phase change problems can be characterized into Euler method and Lagrangian method. The front track method was used to simulate horizontal film boiling (Juric and Tryggvason, 1998). Source terms were used in the continuity equation and the energy

equation to calculate heat transfer due to phase change on the interface. Level set method was developed to perform simulations of axisymmetric horizontal film boiling (Son and Dhir, 1998). The VOF method was also used to simulate flows with phase change (Welch and Wilson, 2000). Nucleate boiling was simulated using a mesh-free method (MPS-MAFL) (Yoon et al., 2001). Compared with Eulerian methods, the MPS method takes the advantage of calculating heat transfer near the interface directly without measuring the normal vector on the interface. The present hybrid method is extended for the phase change calculation.

To calculate heat transfer using the hybrid method, the following energy equation is solved:

$$\frac{\partial(\rho h)}{\partial t} + \nabla \cdot (\rho h \vec{u}) = \nabla \cdot (\lambda \nabla T) + S_h, \tag{4.42}$$

where h is the specific enthalpy, λ is the thermal conductivity, T is the temperature and S_h is the energy transfer due to phase change given by

$$S_h = \dot{m} h_{lg}, \tag{4.43}$$

where $\dot{m}$ is the phase change rate and h_{lg} is the specific latent heat.

The specific enthalpies are first solved on the mesh grids, and then the specific enthalpies of particles are interpolated from the mesh grids, just as we did for velocities in Section 4.2.1. The solid particle is recognized as a liquid one when its enthalpy increase exceeds the specific latent heat.

4.2.4 Compressible flow calculation

Unified numerical formulation for compressible and incompressible flows is important in practical applications, especially with complex mixture of flows with a wide range of Mach numbers. The CIP method has been developed as a universal numerical technique to solve all the differential equations, while the CUP algorithm was applied in the CIP method

for multi-phase flow simulations (Yabe et al., 2001). In the CIP/MM FVM, the spatial discretization is constructed using two kinds of moments and this enables accurate calculation for advection (Xiao, 2004). However, they need a special procedure to reconstruct interfaces among different phases and numerical diffusion will be caused by fluid convection.

In the present study, the mesh-particle hybrid method is developed for efficient and accurate simulations of mixed compressible and incompressible flows. In this method, the main part of the flows is solved using the CIP/MM FVM coupled with the CUP algorithm, and the interface is simulated using the FVP method without numerical diffusion.

The pressure-based projection is performed by solving the following Poisson equation for pressure:

$$\nabla^2 p^{n+1} = \frac{1}{\Delta t}(-\vec{u}^* \cdot \nabla \rho^{n+1} + \frac{1}{C^2}\frac{p^{n+1} - p^*}{\Delta t} + \nabla \cdot \vec{m}^*), \tag{4.44}$$

where C is the sound speed, p^{n+1} the iterated pressure of the next step, $\vec{u}^*$ the temporal velocity after advection, ρ^{n+1} the density at the next step, p^* the temporal pressure after advection and $\vec{m}^*$ is the temporal momentum after advection. For compressible phase, C is calculated as

$$C = \sqrt{\frac{\gamma p}{\rho}}. \tag{4.45}$$

We can then obtain the updated physical variables for each cell and go to the next step.

4.3 Summary

A computational code using a hybrid method, which couples the CIP/MM FVM and the FVP method was developed for two-phase flow simulations. In this hybrid method,

1. The CIP/MM FVM is used to calculate the main component of the fluid dynamics, and

2. Numerical particles in the FVP method are distributed only over the surface of the liquid to capture interfacial features between liquid and gas phases.

The mesh and particle methods are combined tightly in a single numerical solution algorithm to improve numerical accuracy and stability.

The hybrid method can also be used to perform heat transfer calculations and compressible flow calculations.

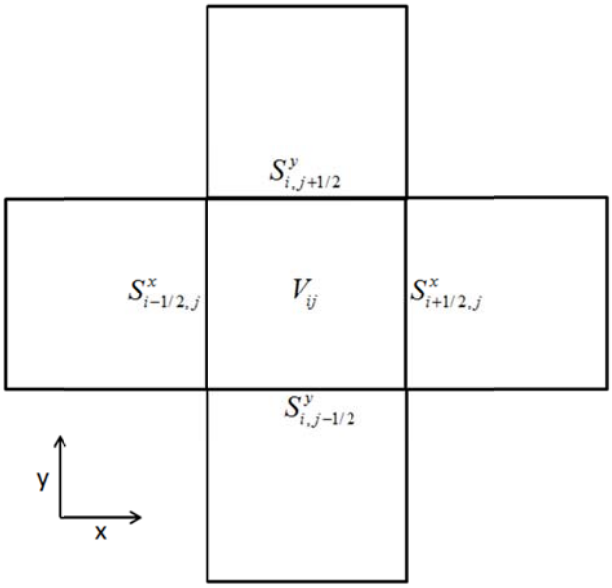

Figure 4.1-1. A 2D control volume in CIP/MM FVM.

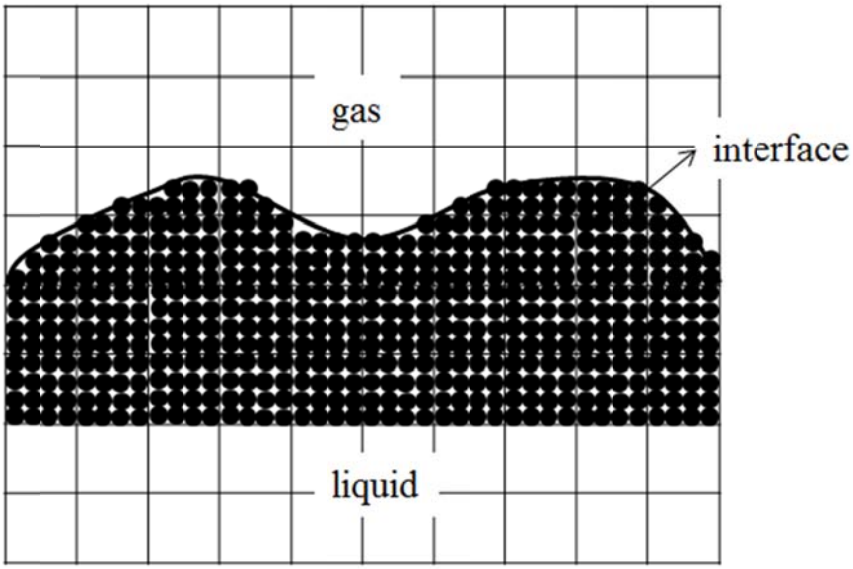

Figure 4.2-1. Distribution of particles and mesh.

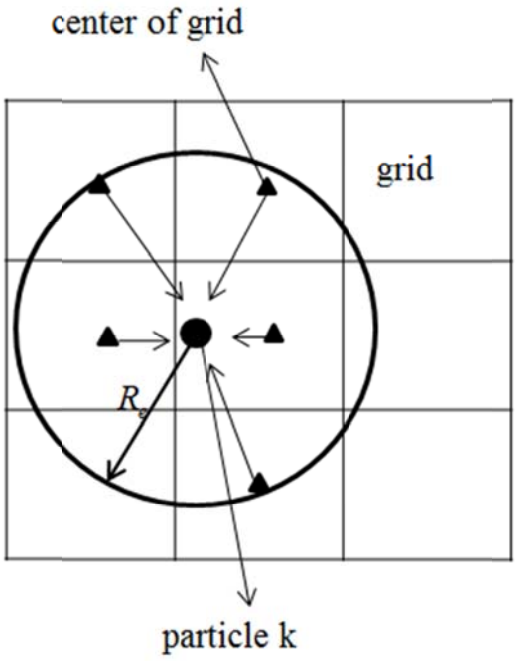

Figure 4.2-2. Interpolation of a velocity from mesh to particle.

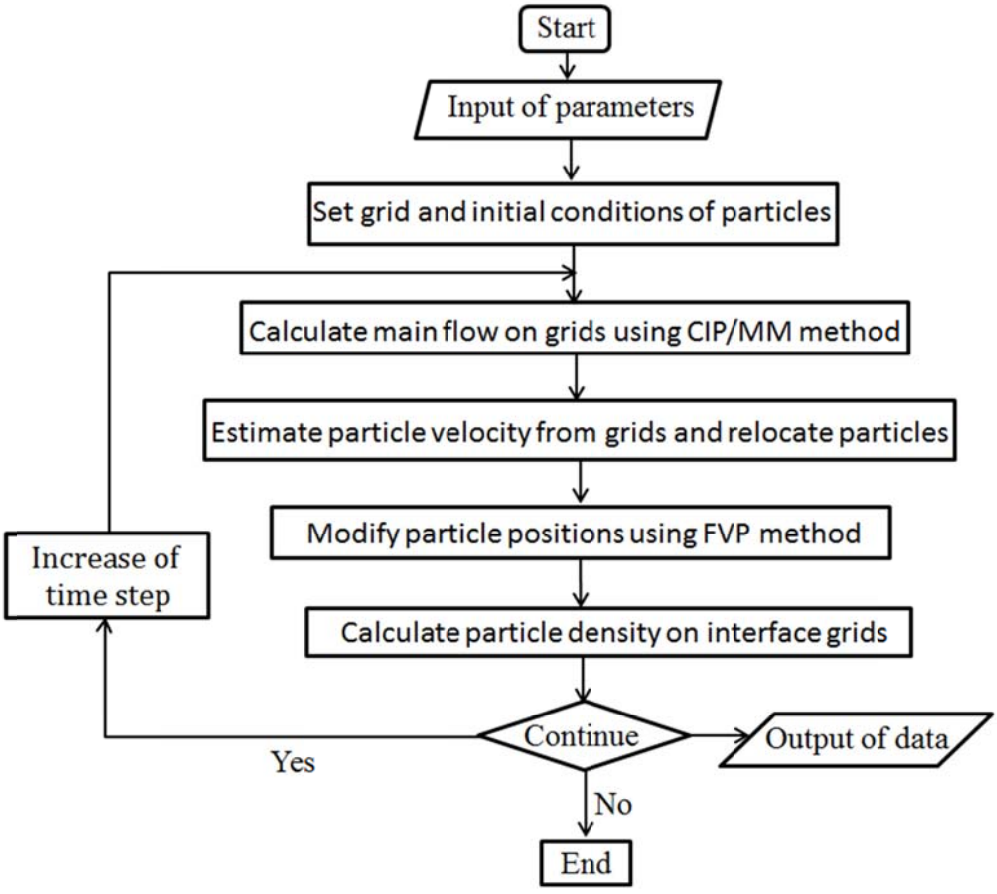

Figure 4.2-3. Numerical algorithm of the present hybrid method.

Chapter 5

Multi-phase Flow Simulations Using Mesh-Particle Hybrid Method

In this Chapter, several benchmark calculations are carried out to validate the developed mesh-particle hybrid method. First one is a dam break problem of water column collapse. It is typical incompressible flow with free surface. Then a single bubble rising problem is simulated to demonstrate the capability of this hybrid method to capture the interface in two-phase flow simulation. We also analyze behavior of bubble breakup induced by velocity difference to demonstrate the ability of the present hybrid method to simulate interface disjunction. Then Stefan problem and the horizontal film boiling problem are calculated to validate the heat transfer model in the hybrid method. Compression of a gas bubble is also simulated to validate the compressible calculation using the hybrid method.

5.1 Simulation of flows with interface deformation

5.1.1 Simulation of water column collapse

The computational domain for the water collapse problem is 10 cm×10 cm as shown in Figure 5.1-1. The initial grid size and particle size were set to 1.0×10^{-2} m and 2.5×10^{-3} m, respectively, and the time step to 1.0×10^{-4} s. The left vertical wall restrains a water column of initial width 2.5 cm and height 5 cm. The density ρ_l and dynamic viscosity μ_l of the liquid phase is that of water set to 999.2 kg/m^3 and 1.138×10^{-2} Pa·s, respectively; the gas phase is air for which we used density ρ_g of 1.225 kg/m^3 and the dynamic viscosity μ_g of

1.776×10^{-5} Pa·s. The surface tension coefficient σ of the liquid phase was chosen as 0.076 N/m. The gravitational acceleration was set to 9.8 m/s^2. In the following, the collapse of the water column, the main part of the flow is represented by the color function of the mesh grid, whereas the interface of the liquid is represented by particles.

The simulation results are shown in Figure 5.1-2. In collapsing, the water body slides to the bottom of the tank, arrives at the right vertical wall after 0.2 s and then rises up the wall. The rising water stops ascending at around 0.3 s and then descends due to gravity. As seen in this figure, the interface surface of the body of water is sharply captured in detail by the numerical particles. The color function of the mesh grid, also shown in Figure 5.1-2, clearly depicts the movement of the liquid.

Figure 5.1-3 compares the results for the developing leading edge of water body between simulation and measurement data (Martin et al., 1952). In this figure, the ordinate represents the leading-edge position from the left wall, while the abscissa indicates the time. Although the comparison shows that the leading edge moves faster in the simulation up until the middle stage of the transient behavior, it agrees very well with the measurements latterly.

We also performed a particle-based simulation using only the FVP method. We used the PISO algorithm to solve the governing equations. In this simulation, particle size was 0.25 mm and the simulation geometry was the same as that for the simulation using the hybrid method. Although the FVP method reproduced the collapsing water behavior, the pressure solution was found to be unstable. This is because after the start of the calculation, the numerical particles were unable to maintain a uniform distribution with a constant particle density, resulting in an increase of numerical error in regard to pressure. In contrast, using the present hybrid method, we obtained a more stable pressure solution. A comparison of the calculated pressure on the bottom of the tank is shown in Figure 5.1-4.

Here, the time variation of the maximum pressure at the bottom of the tank is chosen for comparison. As the water column begins to collapse, the pressure increases rapidly, peaks after 0.1 s, and decreases when the collapsing as the water rushes towards the right wall. Note that the FVP method shows fairly large pressure oscillations even after 0.3 s when water's movement stopped gradually, whereas they are small in the simulation using the present hybrid method. This indicates a distinction in numerical stability for the two methods. And as mesh's size is four times of particle's size and particles only distributed near the surface of the liquid in the hybrid method, compared to the FVP method the present hybrid method required less than one-tenth the computation time.

5.1.2 Simulation of single rising bubble

Figure 5.1-5 depicts the computational domain used in the simulation of the rising air bubble; its dimension is 10.0 cm for both lateral and axial directions. The grid and particle sizes were set to 1 mm and 0.25 mm, respectively. The center of the 2-cm diameter bubble is initially located at a height of 4.0 cm above the bottom of the tank. The properties of the liquid and gas phases are the same as those used in the rising bubble simulation presented in Section 3.2. The gravitational acceleration was set to 9.8 m/s^2.

In this simulation, we also performed for comparison a particle-based simulation using only the FVP method and an Eulerian simulation using the CIP/MM FVM. The FVP method is adapted for gas-liquid two-phase flow simulations, which used a two-step algorithm that calculates the two phases separately to improve numerical stability for systems with large density differences. Details of this numerical algorithm in regard to solving the governing equations are found in Chapter 2. For the FVP and the CIP/MM FVM simulations, particle and grid sizes are the same as those used in the hybrid method.

Figure 5.1-6 shows the typical changes in bubble shape obtained from the FVP, hybrid and the CIP/MM FVM. Under the present conditions, the Eötvös number (see Eq (3.1)) and

the Morton number (see Eq (3.2)) are 51 and 3.7×10^{-7}, respectively. The hybrid and the CIP/MM FVM yielded a skirted bubble shape, whereas the FVP method produced bubble shapes between a skirted shape and a dimpled ellipsoidal-capped shape (as noted in Section 3.2). However, it can be concluded that the present hybrid method as well as the CIP method can reproduce reasonable bubble shapes because it is consistent with the existing experimental data under the present conditions (Grace et al., 1976). Additionally, as numerical particles are only distributed near the interface in the present hybrid method, the computation cost is much less than that of the FVP method. The hybrid method captures the bubble interface more clearly, compared with the CIP/MM FVM. The present result demonstrates the capability of the present hybrid method to simulate changes in topology of the interface accurately and efficiently for two-phase flows with large density and viscosity ratios.

5.1.3 Simulation of droplet breakup

Understanding of the breakup of fluid droplets is important in nuclear safety analysis. In severe accident of nuclear plants, the molten core may form droplet and interact with the coolant in the nuclear plant. Experimental data of liquid droplet breakup have been summarized and many types of breakup modes were commonly observed (Pilch and Erdman, 1987). Numerical analyses of droplet breakup were also carried out. While some aspects of droplet breakup are 3D phenomenon, a 2D simulation can still provide a good deal of insight into the breakup process and may be qualitatively compared with experimental result (Zaleski et al., 1995, Duan et al., 2003).

Droplet breakup behavior is classified by the Weber number. The Weber number represents the ratio of disruptive hydrodynamic force to stabilizing surface tension force:

$$We = \frac{\rho V^2 D}{\sigma}. \tag{5.1}$$

Here, ρ is the density of the continuous fluid, V is the relative velocity between the continuous fluid and the droplet, D is the initial diameter of the droplet and σ is the surface tension. There are five distinct modes of droplet breakup determined by the initial Weber number.

1. Vibrational breakup $We \leq 12$,

2. Bag breakup $12 < We \leq 50$,

3. Bag-and-stamen breakup $50 < We \leq 100$,

4. Sheet stripping $100 < We \leq 350$, and

5. Wave crest stripping followed by catastrophic breakup $We > 350$.

This classification of breakup modes is based on various experiments of droplet breakup in gas-liquid systems. It was also reported that similar modes were observed in liquid-liquid systems. Viscosity effects on the droplet breakup are correlated with the Ohnesorge number (On):

$$On = \frac{\mu_d}{(\rho_d D\sigma)^{0.5}}. \tag{5.2}$$

Here, μ_d and ρ_d are the viscosity and density of the droplet, respectively. It is known that viscosity effects are not significant when On is less than about 0.1 (Krzeczkowski et al., 1980).

Droplet breakup is simulated using the hybrid method in 2D. The droplet material is assumed as molten corium and the continuous fluid is water. The density of the droplet is set to 9,200 kg/m^3, the surface tension is 0.40 N/m, and the viscosity is 2.82×10^4 Pa·s. The density of the continuous fluid is set to 1,000 kg/m^3. The calculation arrangement is depicted in Figure 5.1-7. The initial droplet shape is a circle with the diameter of 9 mm. The Ohrnesorge number is 4.62×10^{-5}. Thus, effects of droplet viscosity are not

significant in this calculation. The droplet moves in the continuous fluid with initial velocity u_0.

There have been vast of methods studying droplet breakup behavior and we observe that the simulation results of Euler method and Lagrangian method show different droplet behavior. The Godunov Marker-Particle Projection Scheme (GMPPS) method has been used to simulate droplet breakup (Bierbrauer and Phillips, 2008). The method is inherently second-order accurate in time and space and possesses several advantages over conventional interface-tracking methods such as VOF or the MAC method.

The Weber numbers were chosen to allow a comparison to the results calculated using the GMPPS method and they varied through three different initial relative velocities V = 0.73, 0.82 and 2.12 m/s, which are correspond to We = 12, 15 and 100, respectively.

Figures 5.1-8 shows the calculation results of droplet shapes and velocity distributions for We = 12. A droplet is decomposed into two large fragments. This behavior is identified as the vibrational breakup and can be related reasonably with the experimental result compared with the results calculated using the GMPPS method. Figures 5.1-9 shows the calculation results of droplet shapes and velocity distributions for a little bit higher Weber number (We = 24). Vortex was formed and rolled up behind the droplet. This process leaded to the development of sheet stripping breakup. A similar simulation result was obtained by the GMPPS method, although the experimental result indicated the bag breakup. Simulations results are expected to become better if much higher grid resolutions are used (Zaleski et al., 1995). Figures 5.1-10 shows the calculation results of droplet shapes and velocity distributions for a much higher Weber number (We = 100), a distinct mode of sheet stripping breakup was simulated consistently with experimental observation.

5.2 Simulations of flows with phase change and compressibility

5.2.1 Heat transfer behavior

(a) Stefan Problem

As shown in Figure 5.2-1, the solid and liquid are considered incompressible and are initially in quiescent equilibrium. The liquid experiences an increase in temperature on the solid boundary and solid will melt due to heat transfer from the liquid side. In this flow, it was assumed that no convection will developed in the fluids, while the interface moves away from the solid boundary.

By applying the Neumann solution to this Stefan problem with the flow considered here, the interface position δ and the temperature distribution in the liquid can be given by the following analytical solutions (Alexiades et al., 1992):

$$\delta(t) = 2\Pi\sqrt{\frac{\lambda t}{\rho c}}, \tag{5.3}$$

$$\frac{T(x,t)-T_{wall}}{T_{melt}-T_{wall}} = \frac{1}{\mathrm{erf}(\Pi)}\mathrm{erf}\left(\frac{x}{2\sqrt{\lambda t/c\rho}}\right), \tag{5.4}$$

where c is the specific heat, T_{wall} and T_{melt} are the wall and melting temperature, respectively, and Π is a solution of the transcendental equation. It is expressed by

$$\Pi \exp(\Pi^2)\,\mathrm{erf}(\Pi) = \frac{c(\mathrm{T}_{wall}-\mathrm{T}_{melt})}{h_{lg}\sqrt{\pi}}, \tag{5.5}$$

where $\mathrm{erf}(x)$ is the error function.

In the simulation, the grid and particle sizes were set to 1.0 mm and 0.25 mm, respectively. The same density, specific heat and thermal conductivity were used for both solid and liquid phases. Their values were set to 10.0 kg/m^3, 200 J/(kg·K) and 0.05 W/(m·K), respectively. The temperature profile was initialized as a simple linear profile with the wall temperature set to 10 K higher than the melting temperature.

Figure 5.2-2 shows the comparison of interface position as a function of time between the analytical solution and the simulation. The simulation result is in good agreement with the analytical solution. The temperature distribution at 0.5 s in the liquid is indicated in Figure 5.2-3. The y axis expresses the dimensionless temperature $(T - T_{wall})/(T_{melt} - T_{wall})$. As can be seen from this figure, the present simulation reproduces the temperature distribution in the liquid reasonably, although the liquid temperature deviates from the analytical solution slightly. This might be caused by the error in evaluation of the heat transfer due to phase change, because of limited spatial resolution in particles. In spite of this deviation, it can be said that this benchmark simulation demonstrates that this hybrid method is applicable to calculate the phase change occurring at the moving interface.

(b) Horizontal film boiling

The horizontal film boiling was simulated to validate the present hybrid method for the phase change with fluid flow. The schematic diagram was shown in Figure 5.2-4. In the simulation, the grid and particle sizes were set to 2.4 mm and 0.6 mm, respectively. The computational domain was 7.8 cm×7.8 cm. The densities of liquid and vapor were set to be 200.0 kg/m^3 and 5.0 kg/m^3, respectively. The specific heat of liquid and vapor were set to be 400 J/(kg·K) and 200 J/(kg·K), respectively. Thermal conductivities of liquid and vapor were set to be 40.0 W/(m·K) and 1.0 W/(m·K), respectively. The surface tension of 0.1 N/m and the latent heat of vaporization of 100 J/kg were used in the present liquid-vapor system. The temperature profile was initialized as a simple linear profile between the liquid and wall temperatures. The liquid was kept under a saturation condition at 500 K, while the wall temperature was 5 K higher than the liquid temperature.

The initial two-phase interface was specified by the void profile with the half cosine wave $\alpha = 0.5 + 0.4\cos(2\pi x / L)$.

Some snapshots of shape change in the vapor film were shown in Figure 5.2-5. The present calculation simulates the vapor bubble formation due to heat transfer and resultant vaporization. The interface change during this process is clearly captured. The formation of vapor bubble in the present simulation is comparable with that obtained by the VOF method (Welch and Wilson, 2000). On the other hand, departure of the vapor bubble for the film does not appear in the present simulation. This differs from the VOF simulation result. In the present hybrid method, the density of mesh grid on the interface is determined according to the distribution of particles using a weight function. Some error could be caused during the coupling process of the CIP and FVP methods. If necessary, a more accurate scheme will be developed to reasonably calculate the density of mesh grid on the interface. Nevertheless, the present results indicate the potential applicability of the proposed hybrid method to the numerical simulation of gas-liquid two-phase flows with phase change.

5.2.2 Compressible flows

In the present study, compression of a gas bubble (Caltagirone et al., 2011) is simulated to validate present numerical method. Figure 5.2-6 shows the computational domain. A bubble with the radius of d = 20 mm is compressed by liquid in a closed square cavity with the length of L = 0.1 m. The densities of bubble and liquid are set to 1.0 kg/m^3 and 1000 kg/m^3, respectively. Liquid flows into the cavity from the four sides with the speed of V_{in} = 0.0025 m/s. The gravity and surface tension were not taken into account in the present simulation. Using the initial bubble volume V_{Ini} , the normalized bubble volume change is calculated by

$$\frac{V(t)}{V_{Ini}} = 1 - \frac{4V_{in}L}{V_{Ini}}t \ . \tag{5.6}$$

In the simulation, the initial grid size and the particle size were set to 1.0×10^{-3} m and 2.5×10^{-4} m, respectively, and the time step to 1.0×10^{-5} s. Comparison of bubble volume between the simulation and analytical results are shown in Figure 5.2-7. The simulation result is in accurate agreement with the analytical result. Snapshots of bubble shape change are indicated in Figure 5.2-8. Particles in the particles' distribution row represent the interface of liquid phase. The bubble was compressed as the liquid flew into the cavity. It can be seen that the interface is clearly captured by numerical particles.

5.3 Summary

Three adiabatic benchmark simulations, that is water column collapse, a single rising air bubble in water and droplet breakup, were performed to validate the developed hybrid method. Three types of interface deformation, free surface, interface in two-phase flow and interface disjunction, are all captured clearly by the hybrid method. Accuracy of the hybrid method is proved by comparing the simulation results with either experimental results or other numerical simulations. Stability of the hybrid method is demonstrated in the simulation of water column collapse by comparing the pressure at the bottom of the tank with the FVP method. And In these benchmark simulations, the present hybrid method required less than one-tenth the computation time of the particle method calculations. It is expected that the present method can be used widely for gas-liquid and liquid-liquid two-phase flow simulations.

The presented hybrid method was developed for two-phase flow simulations with phase change. The heat and mass transfer model is coupled with this hybrid method. The simulation results of the conventional Stefan problem and the horizontal film boiling

demonstrate that the present hybrid method is potentially applicable to simulate two-phase flows with phase change.

The hybrid method was also developed for calculating compressible and incompressible flow simultaneously. The CIP/MM FVM coupled with the CUP algorithm is used to calculate the main component of the fluid dynamics. A benchmark simulation for compression of a gas bubble was performed to validate the present hybrid algorithm. The simulation results demonstrate the accuracy of this method.

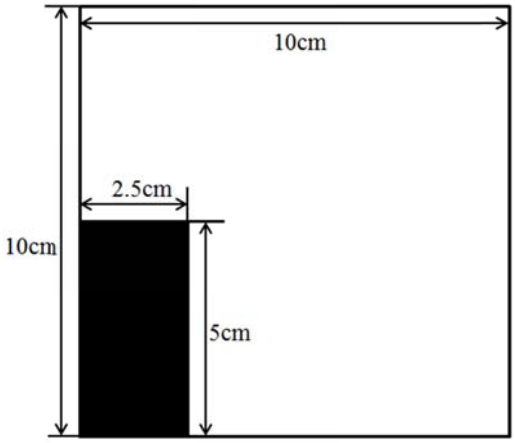

Figure 5.1-1. Geometrical system and initial conditions of water column collapse simulation.

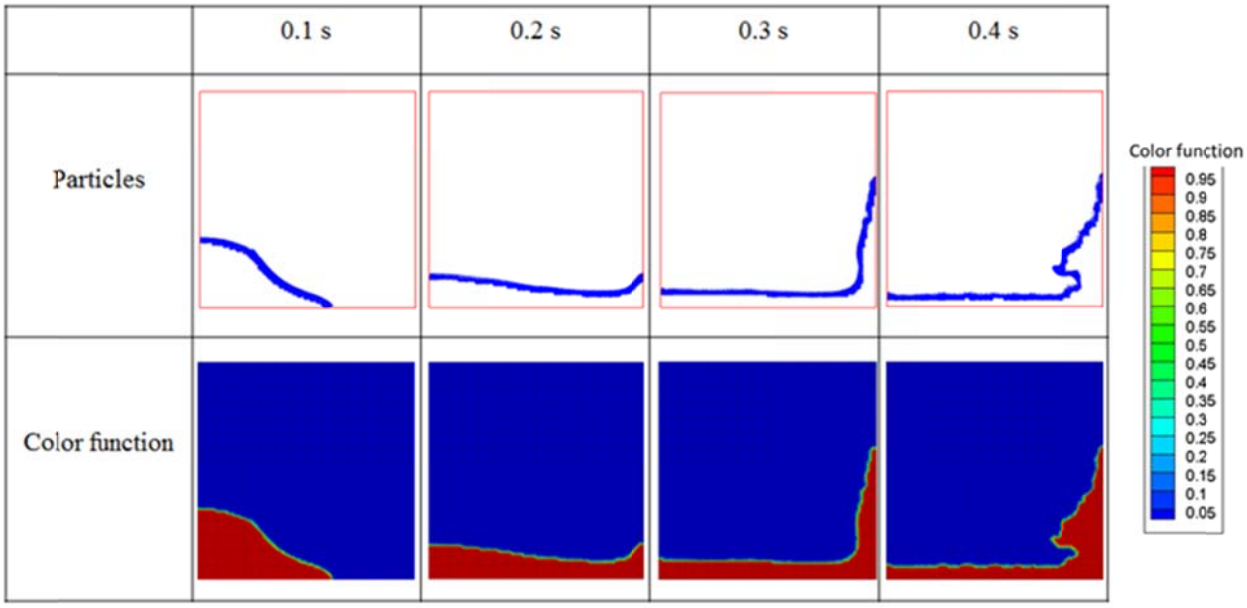

Figure 5.1-2. Distribution of particles on the free surface and color function of mesh grids from the hybrid simulation.

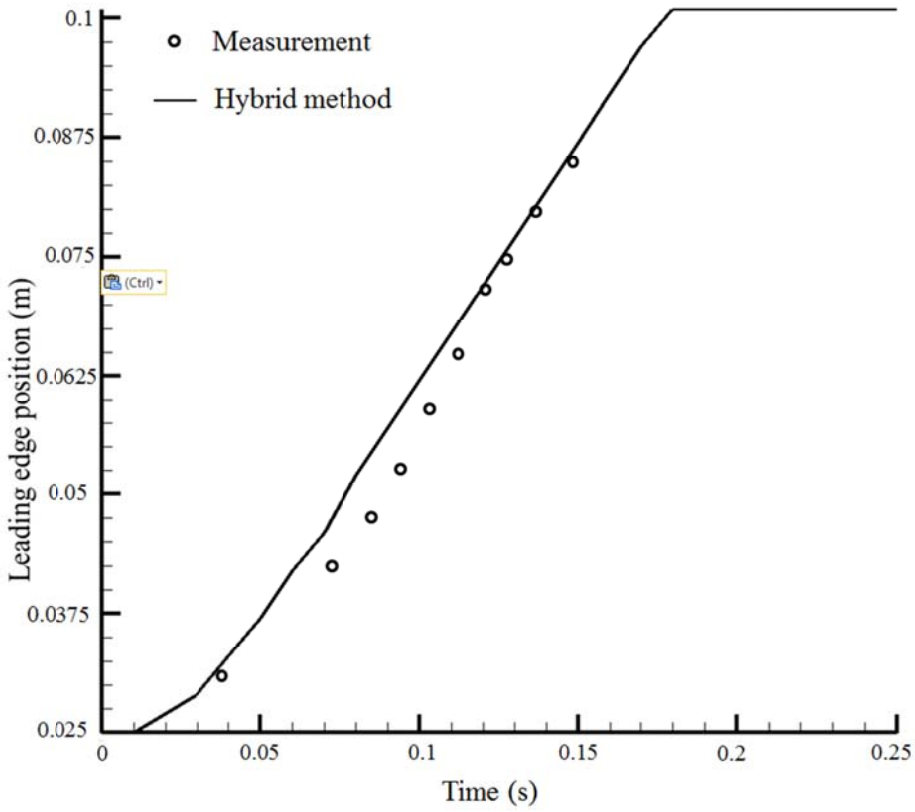

Figure 5.1-3. Position of leading edge after water column collapse.

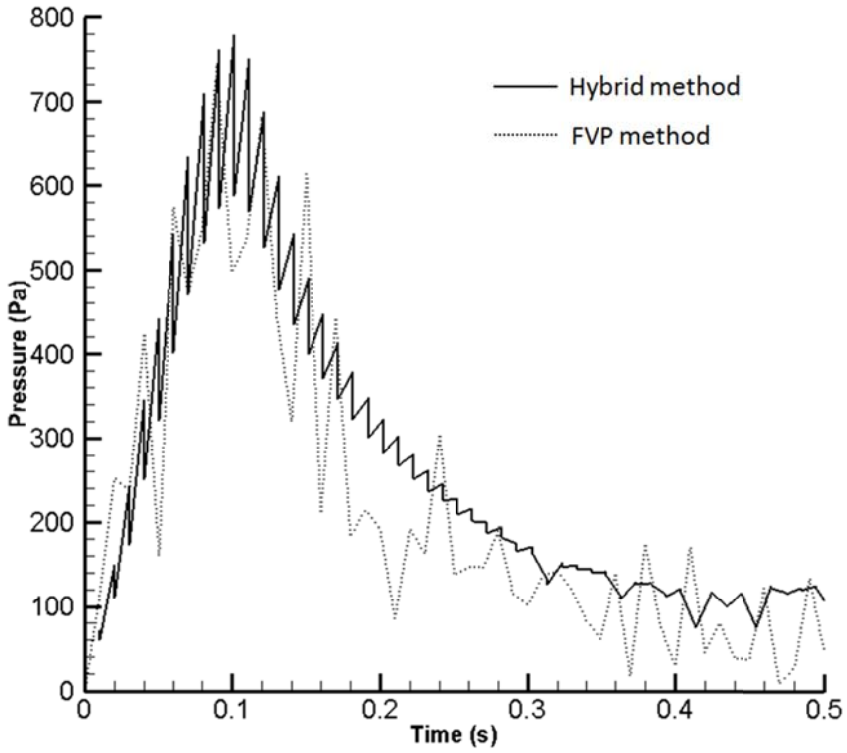

Figure 5.1-4. Maximum pressures at the bottom of the tank.

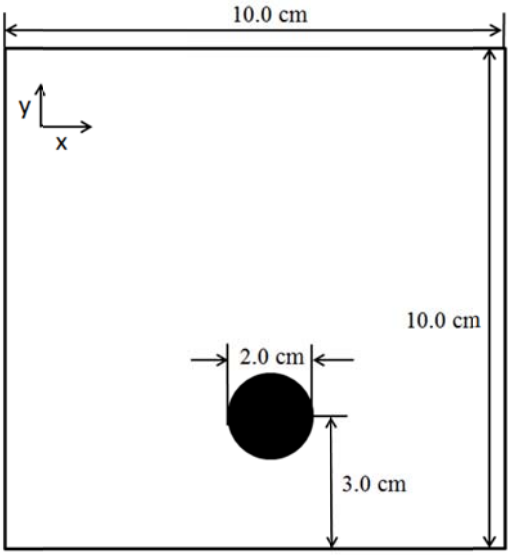

Figure 5.1-5. Geometrical system and initial conditions for the single air bubble simulation.

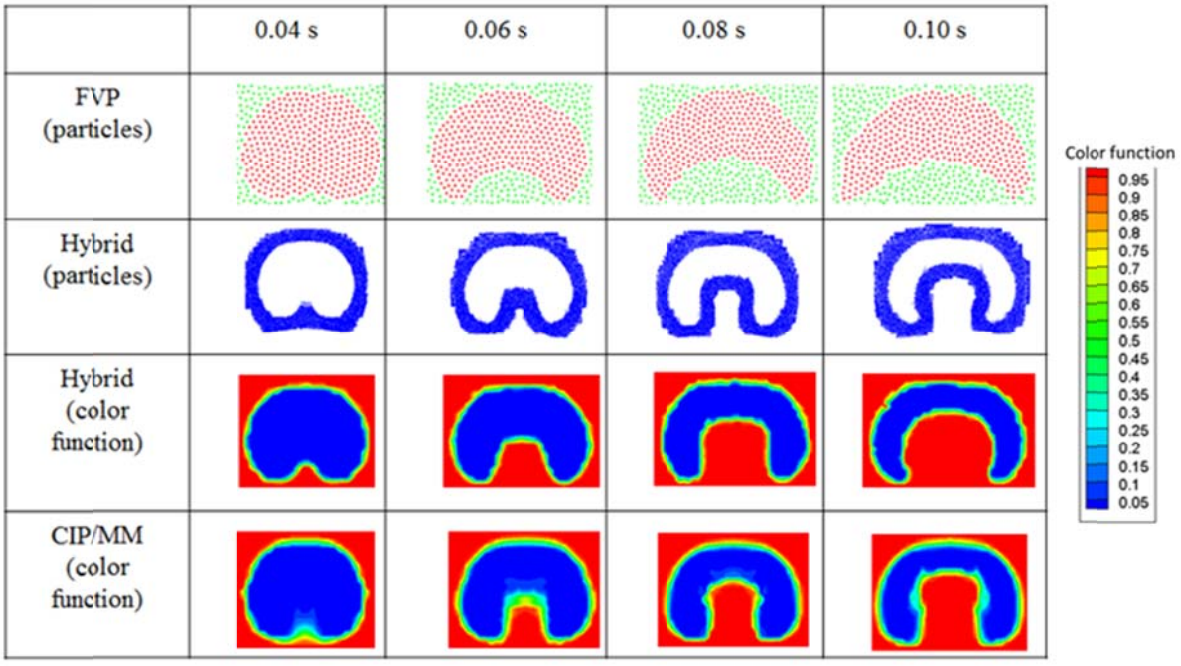

Figure 5.1-6. Snapshots of the shape of an air bubble rising in water using different simulation methods.

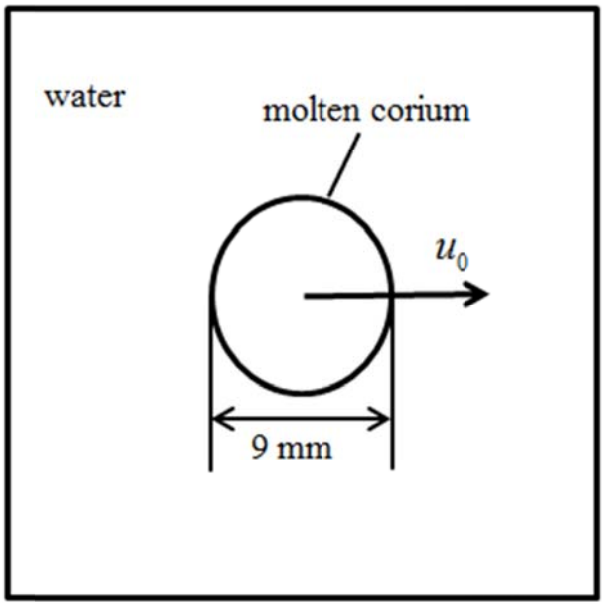

Figure 5.1-7 Schematic diagram of the computational domain for 2D droplet breakup

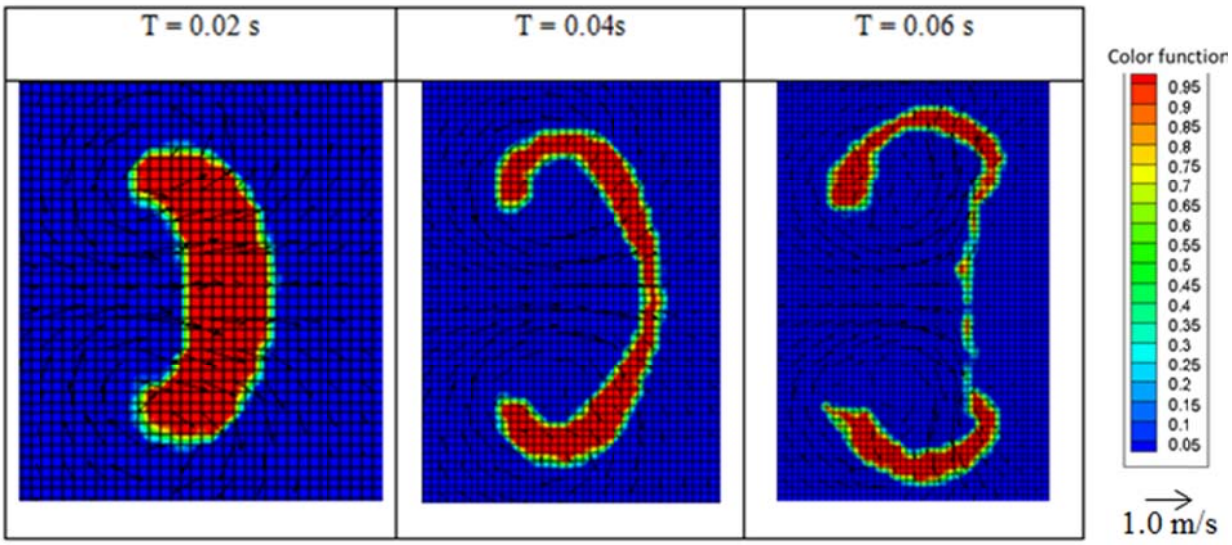

Figure 5.1-8 Droplet breakup behavior for an initial Weber number of 12 (t = 0.02 s, 0.04 s and 0.06 s).

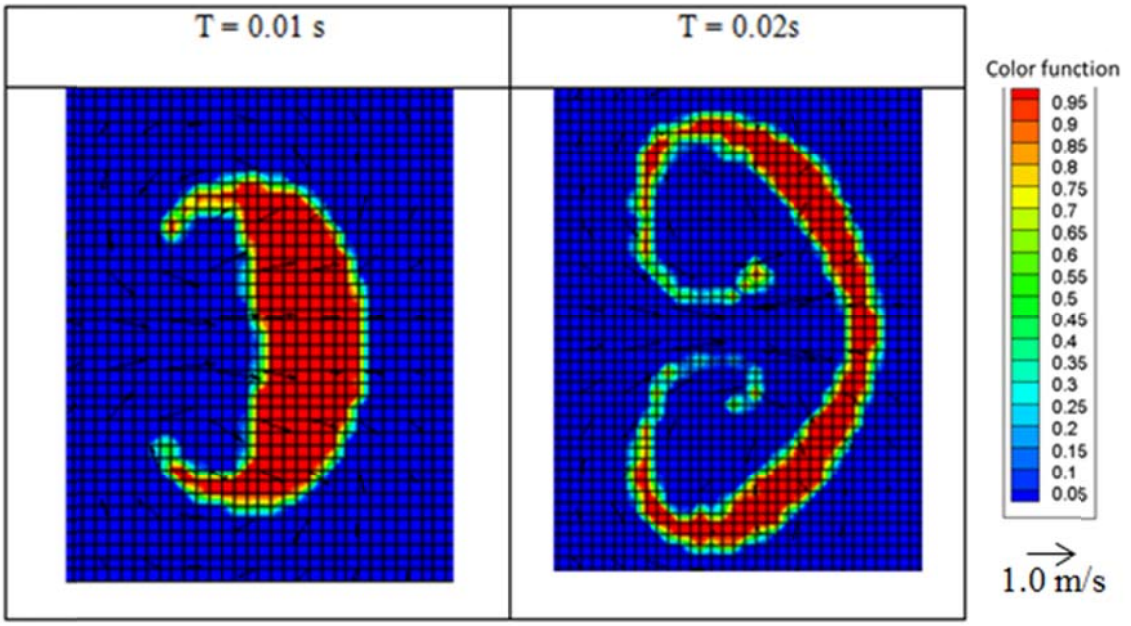

Figure 5.1-9 Droplet breakup behavior for an initial Weber number of 24 (t = 0.01 s and 0.02 s).

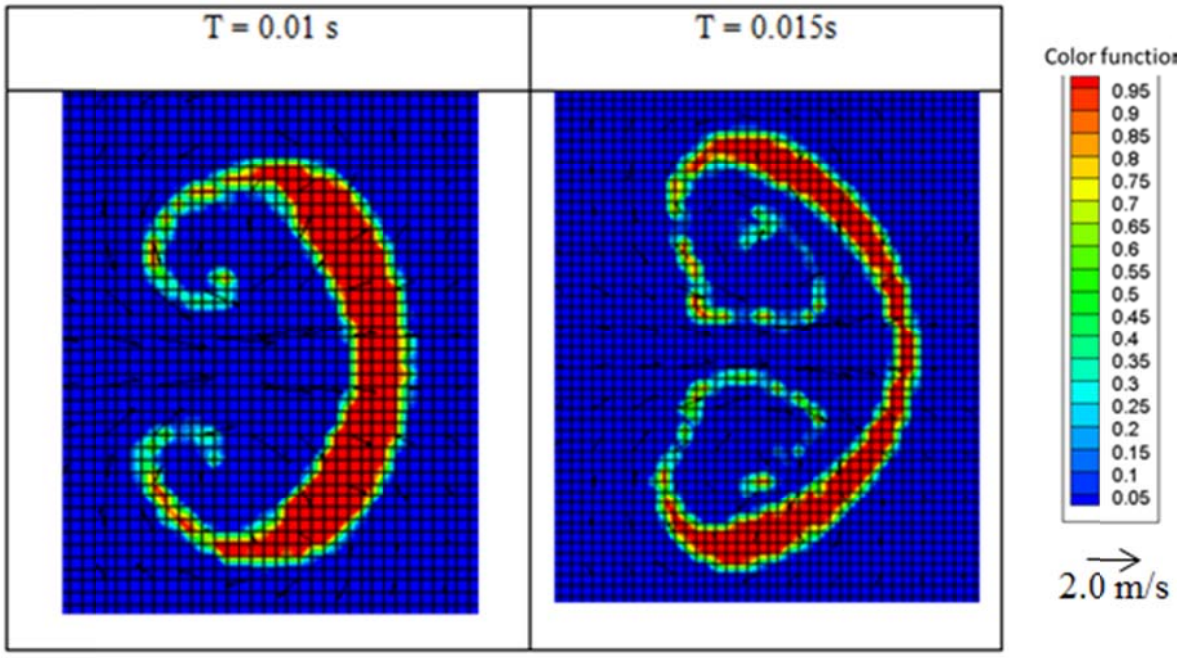

Figure 5.1-10 Droplet breakup behavior for an initial Weber number of 100 (t = 0.01 s and 0.015 s).

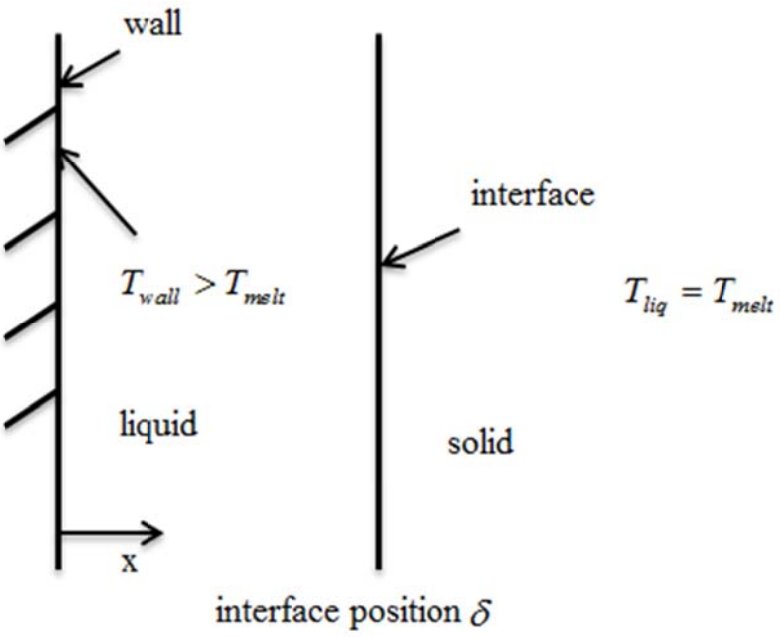

Figure 5.2-1 Schematic diagram of Stefan problem.

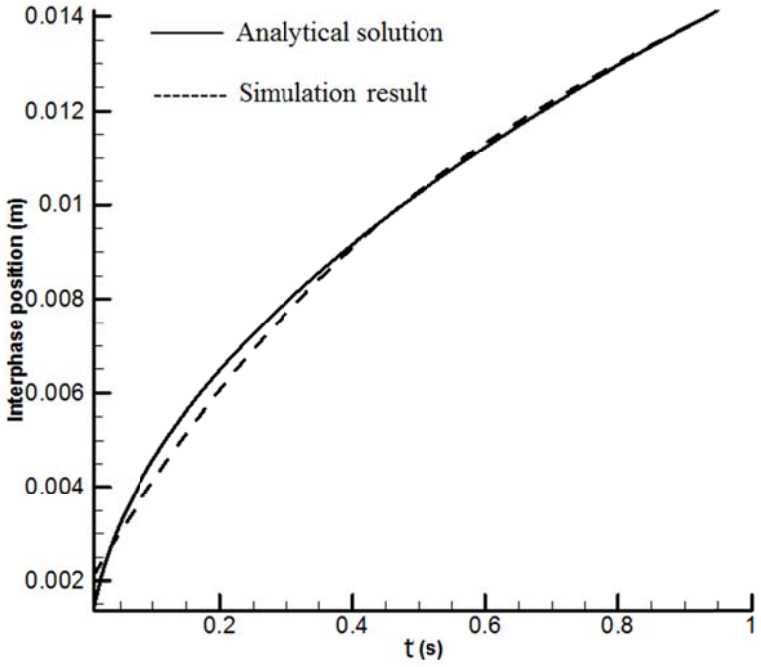

Figure 5.2-2 Interphase position in Stefan Problem.

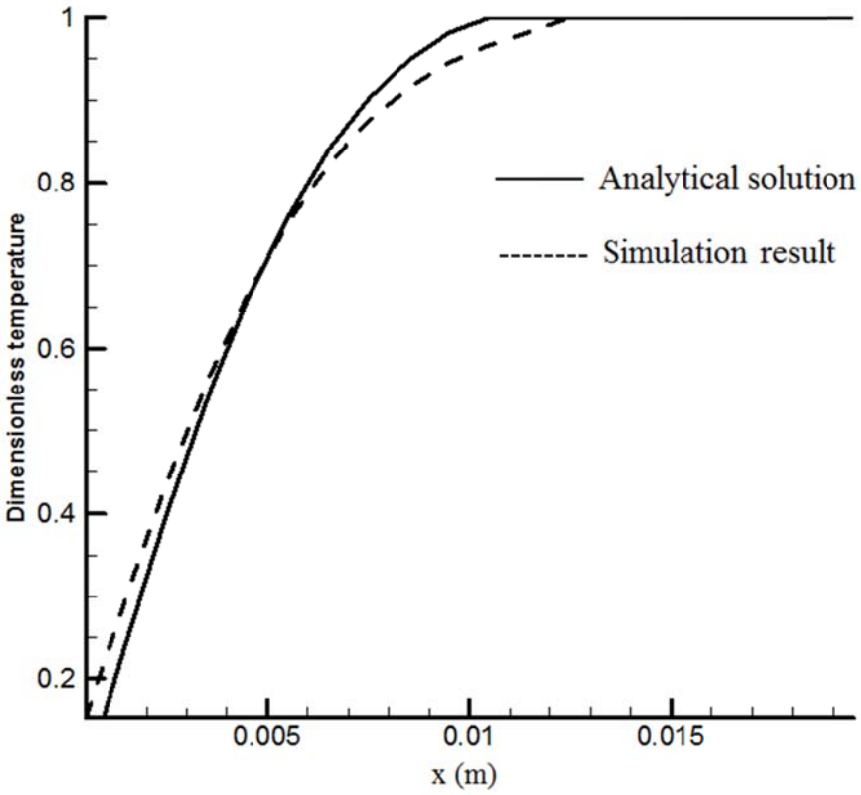

Figure 5.2-3 Temperature distribution at 0.5 s in Stefan problem.

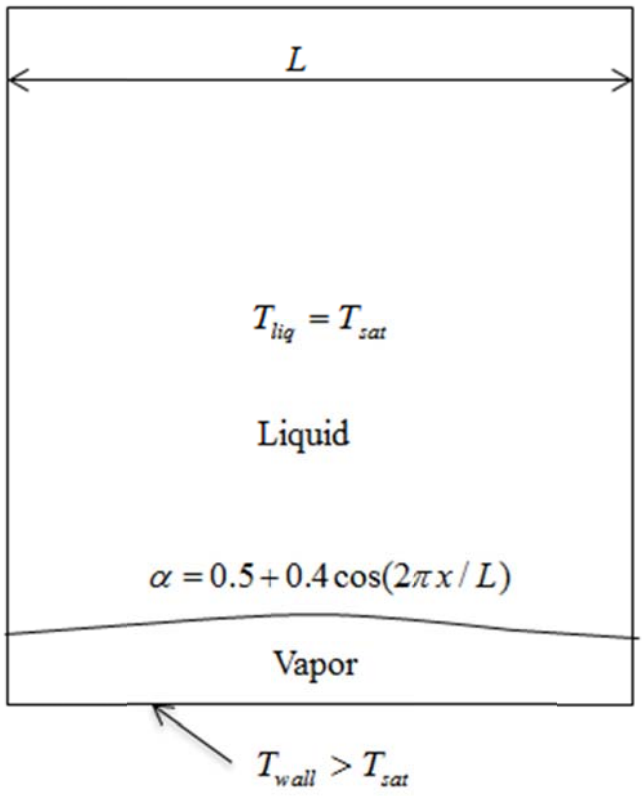

Figure 5.2-4 Schematic diagram of horizontal film boiling.

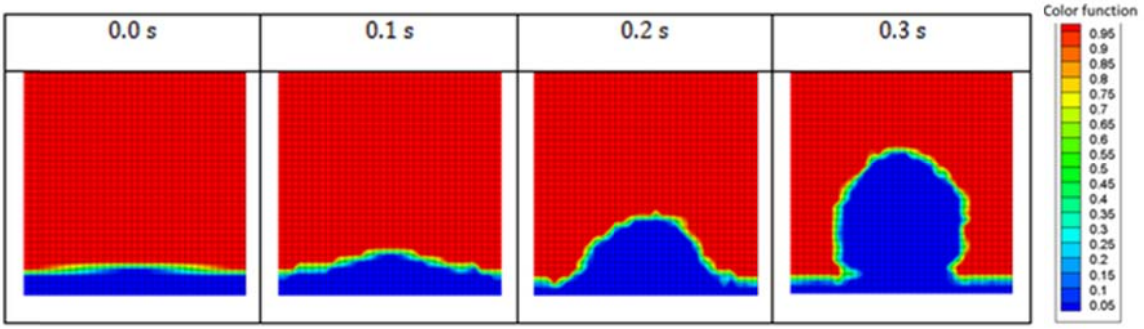

Figure 5.2-5 Snapshots of shape change in vapor film in hybrid simulation.

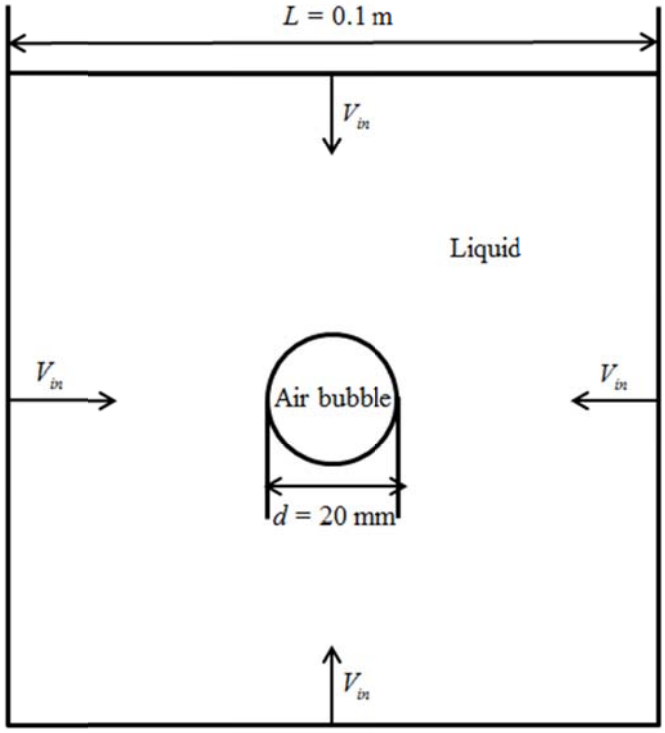

Figure 5.2-6 Computational domain of the compression of a gas bubble.

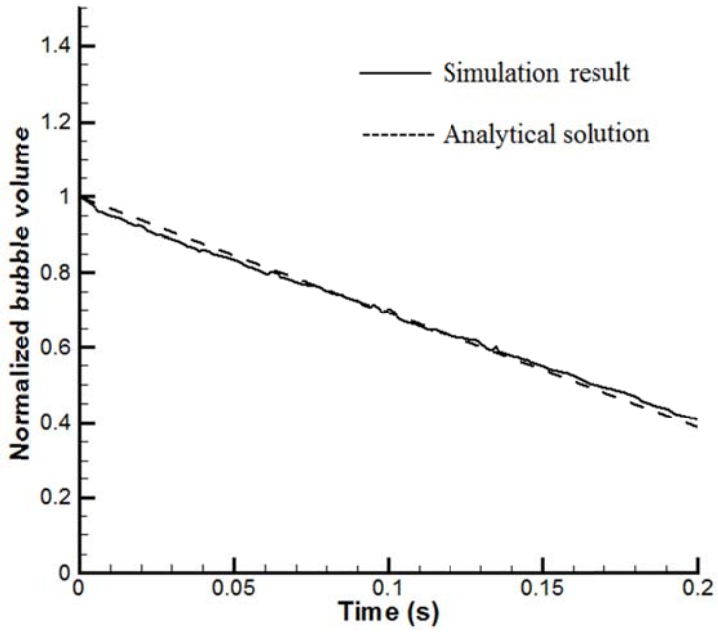

Figure 5.2-7 Normalized bubble volume change.

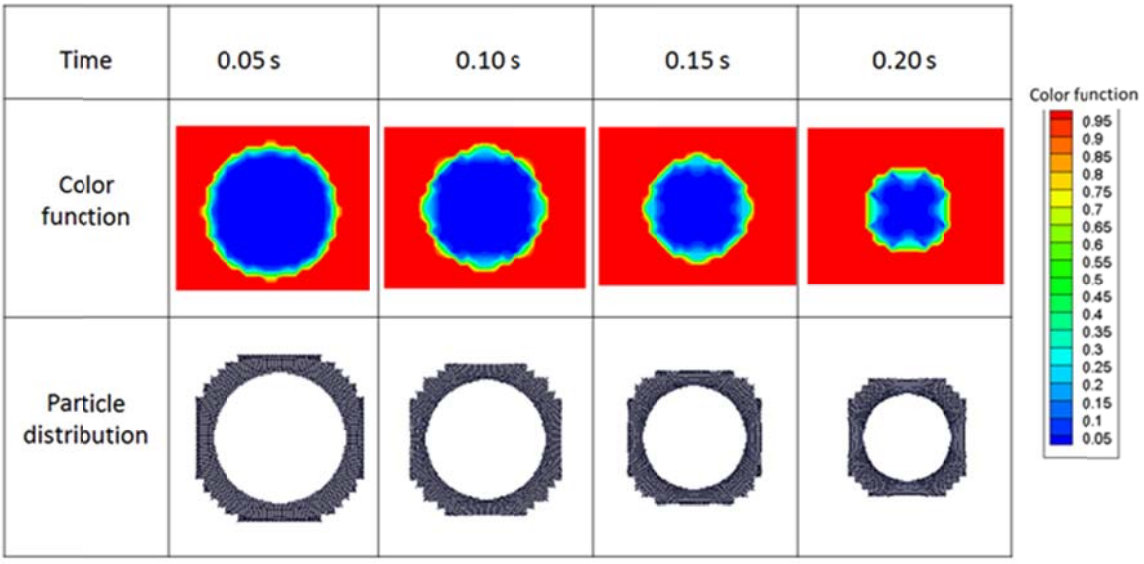

Figure 5.2-8 Snapshots of gas bubble compression in simulation results.

Chapter 6

Conclusions and Future Work

6.1 Conclusions

In this study, the FVP method has been developed to simulate gas-liquid and gas-liquid-solid multi-phase flows. A mesh-particle hybrid method has been also developed to simulate multi-phase flows with interface deformation and to calculate heat transfer and compressible flows. The main outcome of the present study is summarized as follow:

1. A two-step pressure algorithm was developed for the FVP method to enhance the stability when simulate multi-phase flows. Simulations of single bubble rising in stagnant liquid pool over a large range of parameters were performed using the developed FVP method. The results on terminal bubble shapes as well as terminal bubble velocities are in reasonable agreement with conventional experimental data.
2. By coupling with the DEM, the FVP method was used to study the dynamic behavior of multi-phase flows in a gas-solid-liquid mixture system. Models to represent hydrodynamic interactions between solid particles and fluid were also studied.
3. A mesh-particle hybrid method, which couples the CIP/MM FVM with the FVP method, was developed to take advantage of both particle method and mesh method for simulations of multi-phase flows with phase change and compressibility.
4. Simulations of flows with interface deformation in water column collapse, single rising bubble and droplet breakup were performed using the hybrid method.

Simulation results of water column collapse and single rising bubble show good agreement with experimental result. Behavior of droplet breakup induced by velocity difference was successfully simulated, and the results are comparable with those calculated by other numerical methods.

5. Heat transfer behavior of the Stefan problem and the horizontal film boiling were calculated using the hybrid method. The results agree with analytical results or other simulation results.
6. Compression of a single bubble was calculated and analytical results on volume change are reproduced well by the hybrid method.
7. In the benchmark simulations, the present hybrid method required less than one-tenth the computation time of the particle method calculations. The present validation comprehensively demonstrates that the developed hybrid method is potentially useful to simulate gas-liquid two-phase flows under various thermal-hydraulic conditions efficiently.

The present study advances multi-phase flow simulations using the FVP method and mesh-particle hybrid method. It is expected that the present extended framework of the FVP method and the hybrid method will make an essential contribution to the development of multi-phase CFD.

6.2 Future works

(1) Accuracy and stability of the FVP method

The two-step algorithm developed the stability of the FVP method. However, the developed FVP method can't simulate skirted bubble shape due to inaccurate pressure calculation. It is possible to consider a more appropriate kernel function and then apply it

to the FVP method to improve simulation precisions. Re-arrangement of particles if necessary might be also a way to improve the accuracy.

(2) Extension to three dimentional calculation

In present study, all the simulations were performed in 2D system. It is expected to extend the developed particle method as well as the hybrid method to 3D system to obtain more reasonable simulation results.

(3) Applications for the nuclear safety analysis

In the present study, the hybrid method was developed to simulate multi-phase flows with phase change and to simulate compressible and incompressible flow simultaneously. Both the two phenomenon are frequently encountered in thermal hydraulic phenomena of nuclear accidents. It is expected that numerical simulations using the hybrid method and the present models will be useful for detailed analyses of complex, thermal hydraulic phenomenon of multi-phase flows, which appears in the field of nuclear safety engineering.

Acknowledgement

I would like to express my sincere thanks to my supervisor, Professor Koji Morita, for his support during the three-year study. His kindness always encourages me, his attitude always motivates me and his guidance always inspires me.

I would like to thank Prof. Nozomu Fujimoto and Prof. Toshiyuki Aoki of Kyushu University for their willingness to act as my examination committee.

I would like to thank Professor Shuai Zhang of Zhejiang University in China for his recommendation to the Morita Lab and also for his comments and discussions throughout this study.

I would like to thank Assistant Professor Tatsuya Matsumoto of Morita Laboratory, who help in administrations.

I would like to thank Dr. Liancheng GUO for his helpful advice and discussions on my research and also for his help on my daily life.

I am grateful to the student members in Morita Lab for their kindness and help. Mr. Tomoya Taketa and Mr. Oshima helped a lot at the beginning of my life in Japan. And owing to the work of Mr. Ichiro Miya and Mr. Yuki Aramaki, I can complete the study on three phase flow simulation.

I would like to gratefully acknowledge support from the Ministry of Education, Culture, Sports, Science and Technology, Japan under the MONBUKAGAKUSHO Scholarship.

Finally I would thank my family for their supports and encouragements throughout these years.

Abbreviation

CIP	Constrained interpolation profile
CIP/MM FVM	Constrained interpolation profile/multi-moment finite volume method
CSF	Continuum surface force
CUP	Combined, unified procedure
DEM	Distinct element method
FVP	Finite volume particle
GMPPS	Godunov Marker-Particle Projection Scheme
MPS	Moving particle semi-implicit
N-S	Navier-Stokes
PISO	Pressure implicit splitting of operators
PMS	Passively moving solid
SPH	Smoothed particle hydrodynamics
SIA	Surface integrated average
T-F MPS	Two-phase moving particle semi-implicit
VIA	Volume integrated average
VOF	Volume of fluid

Nomenclature

c	specific heat capacity at constant pressure J/kg· K
C	speed of sound, m/s
C_d	drag coefficient
d	bubble diameter, m
e	potential energy function
E	elastic modulus
Eo	Eötvös number
$\vec{f}$	other forces per unit volume, N/m^3
$\vec{f}_{fs}$	solid–fluid interaction force
$\vec{F}$	solid interaction force
$\vec{g}$	gravity force, m/s^2
G	shear modulus
h	specific enthalpy, J/kg
L	width of the calculation domain, m
$\vec{m}$	momentum, kg·m/s
M	Morton number
N	total number of gas particles
Num	number of numerical particles
n^0	initial number density of the particles
$\vec{n}$	unit normal vector
On	Ohnesorge number

p pressure, Pa

P potential energy, J

$\vec{r}$ particle position vector, m

r_e cut-off radius of kernel function or weight function, m

R radius of control volume, m

Re Reynolds number

S particle surface area, m^2

t time, s

$\vec{t}$ unit tangential vector

T temperature, K

$\vec{u}$ velocity, m/s

α_g void fraction

V particle volume, m^3

V_t bubble rising terminal velocity, m/s

We Weber number

w_{ij} kernel function

Greek Letters

α volume fraction of solid particles in the mixture

β momentum exchange coefficient

λ thermal conductivity W/(m·K)

ι shifting magnitude

γ_n damping coefficients in normal direction

γ_s damping coefficients in tangent direction

Δl initial distance between adjacent particles

ε adjustable parameter

ϕ arbitrary scalar function

μ viscosity coefficient, Pa·s

μ_{eff} apparent viscosity, Pa·s

υ Poisson's ratio

η friction coefficient

χ slope of the interpolation function at the cell center

κ curvature of the interface

Π a solution of the transcendental equation

θ color function

ρ density, kg/m^3

σ surface tension coefficient, N/m

ω weight function

ψ repulsive force per unit volume, N/m^3

Subscripts

f fluid

g gas phase

i particle i

ij between particles i and j

I interface between gas and liquid phases

j particle j

l liquid phase

p particle

s surface or solid phase

Superscript

n time step

V volume-integrated average

S surface-integrated average

References

Alexiades V. Mathematical modeling of melting and freezing processes. CRC Press, 1992.

Amsden A A, Harlow F H. The SMAC method: a numerical technique for calculating incompressible fluid flows. Los Alamos Scientific Lab., N. Mex., 1970.

Balevičius R, Kačianauskas R, Mróz Z, et al. Discrete-particle investigation of friction effect in filling and unsteady/steady discharge in three-dimensional wedge-shaped hopper. Powder Technology, 2008, 187(2): 159-174.

Bierbrauer F, Phillips T N. The numerical prediction of droplet deformation and break‐up using the Godunov marker‐particle projection scheme. International journal for numerical methods in fluids, 2008, 56(8): 1155-1160.

Bonometti T, Magnaudet J. Transition from spherical cap to toroidal bubbles. Physics of Fluids (1994-present), 2006, 18(5): 052102.

Brackbill J U, Kothe D B, Zemach C. A continuum method for modeling surface tension. Journal of computational physics, 1992, 100(2): 335-354.

Caltagirone J P, Vincent S, Caruyer C. A multiphase compressible model for the simulation of multiphase flows. Computers & Fluids, 2011, 50(1): 24-34.

Chen C, Xiao F. Shallow water model on cubed-sphere by multi-moment finite volume method. Journal of Computational Physics, 2008, 227(10): 5019-5044.

Chen L, Garimella S V, Reizes J A, et al. The development of a bubble rising in a viscous liquid. Journal of Fluid Mechanics, 1999, 387: 61-96.

Ding J, Gidaspow D. A bubbling fluidization model using kinetic theory of granular flow. AIChE Journal, 1990, 36(4): 523-538.

Duan R Q, Koshizuka S, Oka Y. Numerical and theoretical investigation of effect of density ratio on the critical Weber number of droplet breakup. Journal of Nuclear Science and Technology, 2003, 40:501–508.

Duan R Q, Koshizuka S, Oka Y. Two-dimensional simulation of drop deformation and breakup at around the critical Weber number. Nuclear engineering and design, 2003, 225(1): 37-48.

Ergun S. Fluid flow through packed columns. Chemical engineering progress, 1952, 48.

Frankel N A, Acrivos A. On the viscosity of a concentrated suspension of solid spheres. Chemical Engineering Science, 1967, 22(6): 847-853.

Gidaspow D. Multiphase flow and fluidization: continuum and kinetic theory descriptions. Academic press, 1994, San Diego.

Gingold R A, Monaghan J J. Smoothed particle hydrodynamics: theory and application to non-spherical stars. Monthly notices of the royal astronomical society, 1977, 181(3): 375-389.

Grace J R, Wairegi T, Nguyen T H. Shapes and velocities of single drops and bubbles moving freely through immiscible liquids. Trans. Inst. Chem. Eng, 1976, 54(3): 167-173.

Grenier N, Antuono M, Colagrossi A, et al. An Hamiltonian interface SPH formulation for multi-fluid and free surface flows. Journal of Computational Physics, 2009, 228(22): 8380-8393.

Han J, Tryggvason G, Energy transfer in the secondary breakup of liquid drops, ASME 2000 Fluids Engineering Division Summer Meeting, June 11–15, 2000, Boston, FEDSM2000-11137.

Harlow F H, Welch J H. Numerical calculation of time dependent viscous incompressible flow of fluid with free surface, Physics of Fluids, 1965, 8: 2182-2189.

Hirt CW, Nichols BD. Volume of fluid (VOF) method or the dynamics of free boundaries. Journal of Computational Physics 1981; 39(1): 201–225.

Hua J, Stene J F, Lin P. Numerical simulation of 3D bubbles rising in viscous liquids using a front tracking method. Journal of Computational Physics, 2008, 227(6): 3358-3382.

Huang C, Sheu T W H, Ishikawa T, et al. Development of a Particle Interaction Kernel for Convection-Diffusion Scalar Transport Equation. Numerical Heat Transfer, Part B: Fundamentals, 2011, 60(2): 96-115.

Idelsohn S R, Onate E, Del Pin F, et al. Fluid–structure interaction using the particle finite element method. Computer Methods in Applied Mechanics and Engineering, 2006, 195(17): 2100-2123.

Ii S, Xiao F. A global shallow water model using high order multi-moment constrained finite volume method and icosahedral grid. Journal of Computational physics, 2010, 229(5): 1774-1796.

Ii S, Xiao F. High order multi-moment constrained finite volume method. Part I: Basic formulation. Journal of Computational Physics, 2009, 228(10): 3669-3707.

Ishii E, Ishikawa T, Tanabe Y. Hybrid particle/grid method for predicting motion of micro- and macro-free surfaces. Journal of Fluids Engineering, 2006, 128(5): 921–930.

Ishii E, Ishikawa M, Sukegawa Y, et al. Secondary-Drop-Breakup Simulation Integrated With Fuel-Breakup Simulation Near Injector Outlet. Journal of fluids engineering, 2011, 133(8).

Issa R I, Gosman A D, Watkins A P. The computation of compressible and incompressible recirculating flows by a non-iterative implicit scheme. Journal of Computational Physics, 1986, 62(1): 66-82.

Juric D, Tryggvason G. Computations of boiling flows. International Journal of Multiphase Flow, 1998, 24(3): 387-410.

Khayyer A, Gotoh H. Enhancement of performance and stability of MPS mesh-free particle method for multiphase flows characterized by high density ratios. Journal of Computational Physics, 2013, 242: 211-233.

Kondo M, Koshizuka S, Suzuki K, Takimoto M. Surface tension model using inter-particle force in particle method. ASME/JSME 2007 5th Joint Fluids Engineering Conference, 07; 93-98.

Koshizuka S, Tamako H, Oka Y. A particle method for incompressible viscous flow with fluid fragmentation. Computational Fluid Dynamics Journal, 1995, 4: 29-46.

Koshizuka S, Oka Y. Moving-particle semi-implicit method for fragmentation of incompressible fluid. Nuclear Science and Engineering, 1996, 23(3): 421–434.

Koshizuka S, Nobe A, Oka Y. Numerical analysis of breaking waves using the moving particle semi-implicit method. International Journal for Numerical Methods in Fluids, 1998, 26(7): 751-769.

Kurtoglu I O, Lin C L. Lattice Boltzmann study of bubble dynamics. Numerical Heat Transfer, Part B: Fundamentals, 2006, 50(4): 333-351.

Liu X, Guo L, Morita K, Zhang S. Improved simulation of a single bubble rising in stagnant liquid using finite volume particle method. The 24th International Symposium on Transport Phenomena, 2013,Yamaguchi.

Liu J, Koshizuka S, Oka Y. A hybrid particle-mesh method for viscous, incompressible, multiphase flows. Journal of Computational Physics, 2005, 202(1): 65-93.

Martin JC, Moyce WJ. Part IV. An experimental study of the collapse of liquid columns on a rigid horizontal plane. Philosophical Transactions of the Royal Society of London. Series A, Mathematical and Physical Sciences, 1952; 244(882): 312–324.

Monaghan, J.J.: An Introduction to SPH, Computer Physics Communications, 1988, 48:89-96.

Monaghan J J. Smoothed particle hydrodynamics. Reports on Progress in Physics, 2005, 68(8): 1703.

Nomura K, Koshizuka S, Oka Y, Obata H. Numerical Analysis of Droplet Breakup Behavior using Particle Method, Journal of Nuclear Science and Technology, 2001, 38(12):1057-1064.

Pilch M, Erdman C A. Use of breakup time data and velocity history data to predict the maximum size of stable fragments for acceleration-induced breakup of a liquid drop. International journal of multiphase flow, 1987, 13(6): 741-757.

Shirakawa N, Horie H, Yamamoto Y, et al. Development and Verification Study of the Two-fluid Particle Interation Method-Two-phase Flow Analysis Free from Experimental Correlation. Computational Fluid Dynamics Journal, 2001, 9(4): 348-365.

Son G, Dhir V K. Numerical simulation of film boiling near critical pressures with a level set method. Journal of Heat Transfer, 1998, 120(1): 183-192.

Sussman M, Smereka P, Osher S. A level set approach for computing solutions to incompressible two-phase flow. Journal of Computational physics 1994; 114(1): 146–159.

Sussman M, Puckett E G. A coupled level set and volume-of-fluid method for computing 3D and axisymmetric incompressible two-phase flows. Journal of Computational Physics, 2000, 162(2): 301-337.

Tryggvason G, Bunner B, Esmaeeli A, et al. A front-tracking method for the computations of multiphase flow. Journal of Computational Physics, 2001, 169(2): 708-759.

Unverdi S O, Tryggvason G. A front-tracking method for viscous, incompressible, multi-fluid flows. Journal of computational physics, 1992, 100(1): 25-37.

Welch S W J, Wilson J. A volume of fluid based method for fluid flows with phase change. Journal of computational physics, 2000, 160(2): 662-682.

Wen C, Yu Y H. Mechanics of fluidization. Chem. Eng. Prog. Symp. Ser. 2014, 62(62): 100.

Xiao F. Unified formulation for compressible and incompressible flows by using multi-integrated moments I: one-dimensional inviscid compressible flow. Journal of Computational Physics 2004; 195(2): 629–654.

Xie H, Koshizuka S, Oka Y. Modelling of a Single Drop Impact onto Liquid Film using Particle Method, International Journal for Numerical Methods in Fluids, 2004, 45:1009-1023.

Xie H, Koshizuka S, Oka Y. Simulation of Drop Deposition Process in Annular Mist Flow using Three-dimensional Particle Method, Nuclear Engineering and Design, 2005, 235:1687-1697.

Xu R, Stansby P, Laurence D. Accuracy and stability in incompressible SPH (ISPH) based on the projection method and a new approach. Journal of Computational Physics, 2009, 228(18): 6703–6725.

Yabe T, Xiao F, Utsumi T. The Constrained Interpolation Profile Method for Multiphase Analysis. Journal of Computational Physics, 2001, 169(2): 556–593.

Yabushita K, Hibi S. A finite volume particle method for an incompressible fluid flow. Proceedings of Computational Engineering Conference, 2005, 10: 419–421 (in Japanese).

Yoon H Y, Koshizuka S, Oka Y. Direct calculation of bubble growth, departure, and rise in nucleate pool boiling. International Journal of Multiphase Flow, 2001, 27(2): 277-298.

Zaleski S, Li J, Succi S. Two-dimensional Navier–Stokes simulation of deformation and breakup of liquid patches. Physical Review Letters, 1995, 75:244–247.

Zhang S, Guo L C, Morita K, et al. Simulation of single bubble rising up in stagnant liquid pool with finite volume particle method. NTHAS6, Okinawa, Japan, 2008 Nov, 24‐27, N6P1022.

Zhang S, Kuwabara S, Suzuki T, et al. Simulation of solid–fluid mixture flow using moving particle methods. Journal of Computational Physics, 2009, 228(7): 2552-2565.

Zhang S, Morita K, Fukuda K, et al. A new algorithm for surface tension model in moving particle methods. International Journal for Numerical Methods in Fluids, 2007, **55**(3): 225–240.